metals

MDPI

Article

An Approach to Evaluate the Fatigue Life of the Material of Liquefied Gases' Vessels Based on the Time Dependence of Acoustic Emission Parameters: Part 1

Oleg G. Perveitalov [1,*] and Viktor V. Nosov [2]

[1] Department of Oil and Gas Transportation and Storage, Saint Petersburg Mining University, Saint Petersburg 199106, Russia
[2] Department of Metrology, Instrumentation and Quality Management, Saint Petersburg Mining University, Saint Petersburg 199106, Russia; nosov_vv@pers.spmi.ru
* Correspondence: s215092@stud.spmi.ru

Abstract: In the first part of this article devoted to the assessment of the fatigue life of structural steels at low temperatures, a study was conducted on the effect of pre-cycling in a low-cycle fatigue mode on the time dependences of acoustic emission parameters. Commonly used St-3 steel was tested at −60 °C with varying durabilities, after which it was fractured once during static tests. The multilevel acoustic model used made it possible to estimate the structural parameter γ at the stage of elastoplastic deformation. The stage of active development of microcracks and their coalescence corresponds to a homogeneous fracture with stable acoustic emission characteristics (signal duration, amplitude variation coefficient, etc.). It was shown that regardless of the maximum voltage (460, 480, and 500 MPa) in the cycle and the operating times of up to 0.3, 0.5, and 0.7, the structural parameter remains within the known limits. The parameters of the Weibull law distribution and the logarithmically normal distribution for the coefficient γ were obtained, theoretical and calculated fatigue curves were plotted, and a method was proposed for evaluating the number of cycles before fracture under irregular loading conditions in the real operation of pressure vessels based on the "rainflow" cycles counting method.

Keywords: fatigue; pressure vessel; acoustic emission; AE count; thermal activation; microcracks; hydraulic testing; elastic plastic deformation; stress concentration

check for updates

Academic Editor: Guoqin Sun

Received: 5 January 2025
Revised: 23 January 2025
Accepted: 28 January 2025
Published: 31 January 2025

Citation: Perveitalov, O.G.; Nosov, V.V. An Approach to Evaluate the Fatigue Life of the Material of Liquefied Gases' Vessels Based on the Time Dependence of Acoustic Emission Parameters: Part 1. *Metals* **2025**, *15*, 148. https://doi.org/10.3390/met15020148

Copyright: © 2025 by the authors. Licensee MDPI, Basel, Switzerland. This article is an open access article distributed under the terms and conditions of the Creative Commons Attribution (CC BY) license (https://creativecommons.org/licenses/by/4.0/).

1. Introduction

The oil and gas transportation system is under high loading conditions, and the infrastructure involved in it is developing. This, in turn, is related to the processes of hydrocarbon extraction, field development, and transportation [1–3]. The increase in the number of new main pipelines, technological pipelines, pressure vessels for gas storage and transportation, storage tanks for liquefied petroleum gasses and LNG, isothermal tanks, and the construction of new tankers for gas transportation during low-temperature storage, as well as the growing wear of existing equipment for the transportation and storage of hydrocarbons sets the task of developing methods for a physically proven assessment and prolongation of the remaining fatigue life of such facilities. The tool in this case is periodic testing and constant monitoring of structural integrity [4]. An important place in this engineering direction is occupied by predicting the fatigue life of low-temperature LPG and LNG storage facilities due to the special mechanism of damage accumulation, kinetics, and the final act of destruction of their material elements, taking into account the specifics

of the operation of such equipment [5]. The effect of low temperatures on the destruction features of such objects can be divided into the effects of low ambient temperatures and cryogenic temperatures of the stored liquefied product on the pipeline or vessel material. The first factor is related to the development of the Arctic as a strategically important region for the transport of oil, natural gas and associated petroleum gas [6] and the second factor is related to the growing share of LNG in all gas exports.

Most real industrial facilities are operated under cyclic loading conditions with different cycle forms. The evaluation of fatigue life is one of the most important tasks of ensuring safety in mechanical engineering and extending the inter-repair period [7,8]. Pressure vessels, pipelines, and cryogenic tanks operate under conditions of periodic changes in operating pressure, thermal fluctuations, and the presence of an aggressive environment. The most widely used mode of operation with variable loading is the "two-shift" mode, which includes a daily start and stop cycle. Under such cyclic loading conditions, short-term thermal stress [9], especially in facilities such as heat exchangers [10], can lead to fatigue fracture over a small number of cycles, especially in large cross-section elements [11]. For example, for main oil pipelines, the average number of cycles of performance drop per year is 300–350 [12,13]. In addition, structural elements experience cyclic loading when the system moves from one set of loads in terms of pressure, temperature, torque, and force to another set of loads [14–16]. The effects of these types of cyclic loading changes are similar to the results of fatigue tests for multi-cycle and low-cycle loads [11].

Low operating temperatures contribute to the nature of the destruction. First of all, this is manifested in the predominance of the destructive component, namely the accumulation of microcracks [17,18] and the development of macrocracks. For example, according to the results of a survey of 160 reservoirs in the North region, it was found that 40% of fractures occurred in the coldest months [19]. Half of all detected defects were crack-like planar discontinuities. The areas of welds represented a particularly dangerous zone [20]. The same was shown on the gas pipelines of the Arctic [21]. At the same time, the transverse section of the structures was characterized by an almost completely brittle surface. There are a number of models for a nonlinear summation of fatigue damage [22], some of which require only fatigue curve data [23]. However, to assess the structural changes that occur during fatigue fracture, methodological approaches are needed that would provide objective information about the kinetics of damage accumulation.

The dependence of durability on temperature and stress is called the time dependence of strength, the temperature–time dependence of strength, or long-term strength. The time dependence of longevity in semi-logarithmic coordinates is linear and has a general analytical form corresponding to the Arrhenius equation.

$$\tau = Ae^{-\alpha\sigma} \tag{1}$$

Based on a large amount of empirical data on the study of the durability of a large number of different solids (including metals and alloys, halide crystals, glass composites, rocks, and polymers) under constant uniaxial tensile stress, a general empirical formula for durability was proposed [24]:

$$\tau = \tau_0 \exp\left[\frac{U_0 - \gamma\sigma(t)}{kT}\right] \tag{2}$$

where τ_0 is a value of the order of the Debye period of atomic vibrations; U_0 is the energy of destruction activation corresponding to the energy of sublimation (separation of an atom and transition of a body to a gaseous state); γ is the parameter of the structural state, which corresponds to the value of the activation volume and expresses the structural heterogeneity

of the specimen material (about $10 \div 10^3$ atomic volumes); $\sigma(t)$ is the rate of stress change on one structural element; k is the Boltzmann constant; and T is the temperature. The form of Equation (2) indicates that the destruction process is thermally activated (like others, such as chemical processes, phase transitions, diffusion, etc.), which is typical for metastable systems with relaxing (passing into a state with reduced free energy) by overcoming a certain energy barrier U through thermal fluctuation.

When using kinetic representations, the most traditional approach is based on the Bailey criterion. Examples of the use of this principle, together with the application of the thermal activated fracture equation for static durability and taking into account the harmonic variation in stresses, are summarized and presented in a number of important studies [25–27]. The task of developing the model is to move from a static form of expression to dynamic stress changes [28–30], which includes, on the one hand, taking into account the features of structural changes during fatigue—the parameter γ and changes in its value during cycling—as well as the introduction of a time function of stresses into Equation (2). Figure 1 shows the difference between the static and cyclic durability of different types of loading.

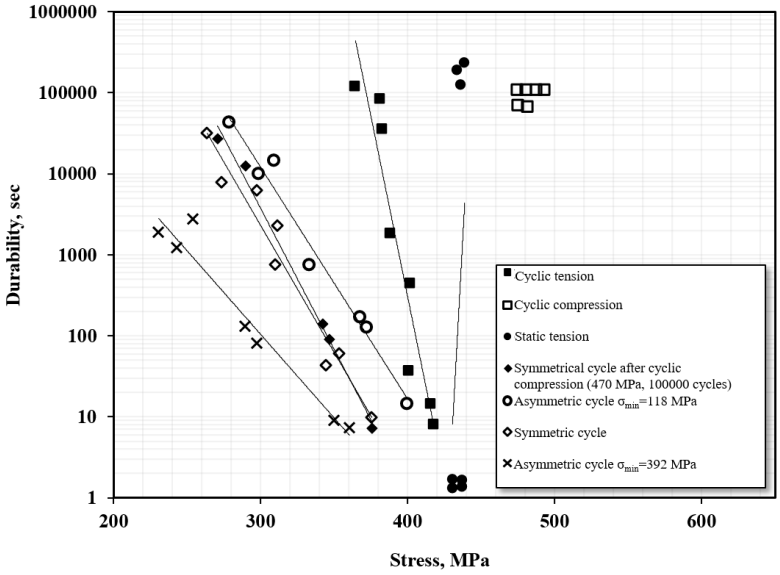

Figure 1. The dependence of durability on stress for various loading modes for St-3 steel (according to [31]).

A distinctive feature of each work is the assessment of the structural parameter and activation energy using various experimental research methods. For example, in [28], tensile tests using thermogravimetric analysis were performed to assess the fatigue life of pure and glass fiber-reinforced polypropylene at room temperature. During these tests, the change in the mass of the specimen over a certain period of time at a constant heating rate was measured to determine the activation energy U_0. The structural parameter γ (lethargy coefficient) was calculated depending on the activation energy. Three models based on the calibration of the Zhurkov model were proposed, including a regression model, a modified strain rate model, and a model based on the lethargy coefficient. The calculated fatigue curves corresponded well to the experimental data.

In [30,32], the fatigue life of HS40R and X20CrMoV121 steels was determined based on the thermally activated fracture equation. The deterministic structure coefficient γ is calculated based on data from creep tests of small specimens and tensile tests and then compared with the experimental one. To estimate the parameter γ and account for its uncertainties, a Monte Carlo sampling approach with a Markov chain based on the Bayesian

model was used. Mahmoudi proposed estimating the fatigue life using the Zhurkov model using an approach that analyzes the accumulation of entropy during the cyclic loading of layered composites T300/EPL1012 [26,33]. Cyclic damage was considered as an increased ability to generate entropy, and the concept of fatigue entropy during destruction was used as a criterion for destruction. It is also proposed to find the lethargy coefficient using data from fatigue curves and the Lambert function, as performed in [33]. Petrov [34] formulated a physical model according to which heat release is a consequence of the kinetic processes of deformation and fracture (crack generation) during thermally activated metastability decay and is considered as a form of excess energy dissipation. Kinetic parameters were determined using operations with heat dissipation, heat capacity, and body heat sink.

2. Materials and Methods

2.1. Experimental Method and Testing Procedure

In accordance with the above technical and production justification, a test program was developed that included mechanical tests for static strength, low-cycle fatigue, and the tension of specimens with concentrators made from a cryogenic tank pipeline. All mechanical tests were carried out with a simultaneous registration of AE signals. The procedure for conducting AE tests included the selection of the material and shape of the specimen, AE equipment, the type and parameters of acoustic emission transducers, methods for attaching sensors to specimens, and the loading protocol. The material was chosen in such a way that, on the one hand, it corresponded to the material of real technological equipment for the transport and storage of gasses in a conventional and liquefied state and, on the other, it most clearly demonstrated the proposed methodology. This equipment includes the main and technological pipelines, pressure vessels, cryogenic tanks and reservoirs, evaporators, and storage equipment for gas transshipment terminals.

To model a situation in which pipelines or tanks are periodically loaded after a certain period of time in operation, low-cycle fatigue tests at low temperatures were performed as part of hydraulic/pneumatic tests. The tests consisted of cyclic loading fractures in order to evaluate the number of cycles at a stress level used, loading a number of specimens to a certain part of the fatigue life, and static single fracture tensile tests of the loaded specimens. The common carbon steel St-3sp was selected as the material. This steel is used in horizontal tanks, pressure vessels and equipment, and welded steel cylinders for LNG. The chemical composition and mechanical properties are given in Tables 1 and 2.

Table 1. Chemical composition of St-3sp steel.

C	*Si*	*Mn*	*Ni*	*S*	*P*	*Cr*	*N*	*Cu*	*As*
0.14–0.22	0.15–0.3	0.4–0.65	$\leq$ 0.3	$\leq$ 0.05	$\leq$ 0.04	$\leq$ 0.3	$\leq$ 0.008	$\leq$ 0.3	$\leq$ 0.08

Table 2. Mechanical properties of St-3sp steel at room temperature.

Property	Ultimate Strength σ_R, MPa	Yield Strength σ_y, MPa	Elastic Modulus E, MPa	Density ρ, kg/m^3	Maximum Elongation in the Central Part, %
Value	472	318	200.17	7.85	42

The cold-breaking properties of Ct3 and its high brittleness temperature make this material the most representative for studying the contribution of embrittlement [35–37] to the process of the low-cycle fatigue of real structures in conditions of limited laboratory tests. For this steel, it becomes possible to study the phenomenon of embrittlement already in the temperature range from 0 to −60 °C [38,39]. At the same time, the material is

common in the field of hydrocarbon transportation. The 5 mm thick specimens were manufactured according to GOST 25.506 [40] and BS EN ISO 12135 [41] in accordance with the requirements for specimens for low-cycle fatigue testing by laser cutting and grinding. In addition, the dimensions of the grippers of the testing machine (the distance from the hole for the gripper rod to the edge of the specimen) were taken into account. The geometric dimensions of the specimens are shown in Figure 2.

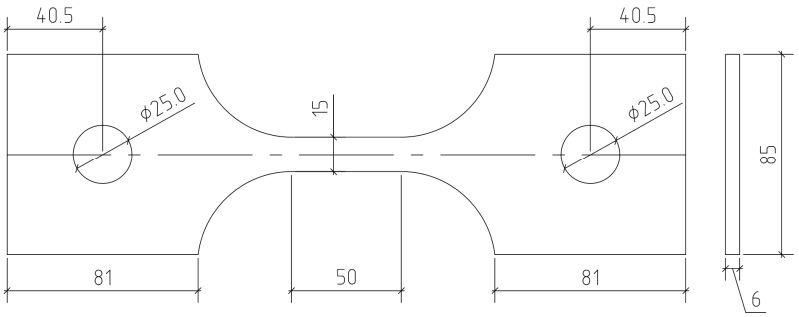

Figure 2. Geometric dimensions of the low-cycle fatigue test specimen.

Cyclic loading tests simulating the loading of an object during the pumping and storage of liquefied gasses were carried out at a temperature of −60 °C in a Zwick/Roell BW91250 thermal chamber (Figure 3a). A cantilever-type mounted dynamic deformation sensor (extensometer) of the Instron DIN 2620-604 model was used. The specimen, fixed in the grips of the machine, was placed in a thermal chamber that was filled with liquid nitrogen vapors while maintaining the desired temperature. Cooling to the required temperature took place in two stages, involving lowering the temperature and holding for 30 min. The lower grip of the machine remained stationary, while the upper one performed cyclic movements with stress control (hard loading). Static and cyclic loading was performed on an Instron 8802 250 kN servo-hydraulic machine (Figure 3a). All mechanical tests were carried out with a pre-set force of 0.5 N to eliminate shear interference from machine parts. Since the tests were carried out at low temperatures, their effects, as well as the presence of ice crystals on the surface of the specimens, did not allow the sensors to be installed directly on the specimen. Waveguides welded to the specimen were used to attach acoustic emission sensors to the specimens. Structurally, the waveguides were a curved rod with a diameter of 4 mm made of stainless steel, at the end of which a steel plate with a diameter of 30 mm and a thickness of 3 mm was welded (Figure 3b). This disk was a platform for installing the AE sensor. The waveguides were bent along the specimen and exited through the gap between the upper grip of the machine and the body of the thermal chamber. To eliminate false AE signals from the impact of the waveguide on the body of the thermal chamber, in this place, the latter was wrapped in soundproof soft tape.

To record acoustic emission signals, a two-channel portable Uniscope system from "Interunis" company, a preamp UNP-01CD, and resonant acoustic emission sensors GT200 Russian-made were used with the following characteristics: bandwidth—100–200 kHz and resonant frequency—180 kHz. The amplitude threshold during the tests was set at 64–66 Db with a gain of 40 Db. Lithol was used as a contact lubricant. The sensors at the end of the waveguide were fixed with adhesive tape. During the test, the standard parameters of acoustic emission were recorded including total AE count, AE count rate, energy, amplitude, etc.

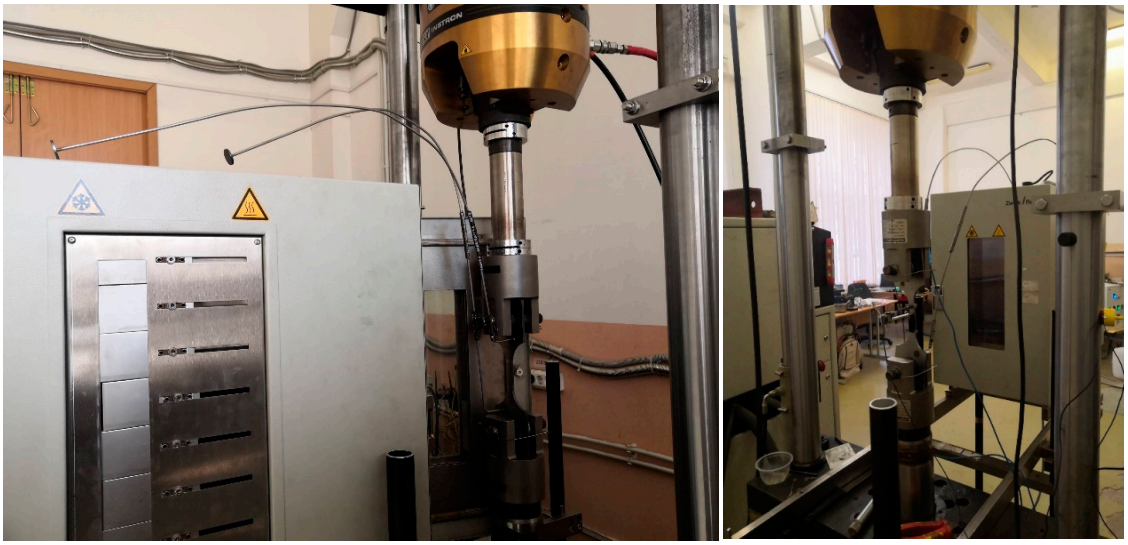

(**a**) (**b**)

Figure 3. Test equipment: (**a**) Instron 8802 250 kN servo-hydraulic machine and Zwick/Roell BW91250 thermal camera; (**b**) arrangement of waveguides on the specimen.

Initially, mechanical properties were determined on two specimens at room temperature (Specimen I) and low temperature (Specimen II), respectively. For room temperature, the yield strengths σ_y and σ_R were 318 and 472 MPa, respectively; for temperatures of −60 °C, the strengths were 386 and 537 MPa, respectively. Based on the values obtained, three loading levels corresponding to low-cycle fatigue were selected. A series of specimens (specimens III, IV, and V) was brought to complete destruction at various levels of maximum loading in the cycle, at 462.5, 480, and 505 MPa and a temperature of 213 K. These stresses correspond to the general concepts of the fatigue curve branch corresponding to low-cycle fatigue fracture in the concentrator zone. Fatigue tests were performed at a frequency of 5 Hz. The cycle asymmetry coefficient was R = 0.01. Before each test, a single tension was performed to the maximum loading in the cycle to determine the yield strength. A sensor monitoring local plastic deformation was installed on the central part of the specimen (Figure 4). Changes in the relative elongation of the specimen, local plastic deformation, and parameters of the hysteresis loop during cyclic loading were recorded.



Figure 4. Specimen location in a thermal chamber with a fixed Instron DIN 2620-604 dynamic deformation sensor (extensometer).

Furthermore, reproducing conditions similar to periodic hydraulic tests, a single destructive tension of these specimens was performed at room temperature at a loading rate with a stress control of 0.5 MPa/sec. The stress control was performed up to 430 MPa. After that, due to safety requirements, the machine switched to deformation control. Thus, during the tests, the entire area of elastic deformation and the initial stage of elastic plastic deformation were passed with stress control at a constant rate of stress increase. Simultaneously with the loading of the specimens, AE signals were recorded. Two additional tests were also performed on the static stretching of specimens without cycling time with stress control at room temperature (Specimen IX) and low temperature (Specimen X).

After the values of the number of cycles to fracture were obtained at these stress levels, 3 more specimens were tested for cyclic loading to a certain part of operating time from the obtained fatigue life, namely specimen VI to the degree of 0.3 of the fatigue life at 462.5 MPa; specimen VII to the degree of 0.5 of the fatigue life at 480 MPa; and specimen VIII up to 0.7% of the fatigue life at 505 MPa. The test frequency remained at 5 Hz. After reaching the specified operating levels, the specimens were unloaded and cooled.

2.2. Acoustic Emission Model

Predicting the durability of a control object is reduced to estimating the time before fracture occurs and is based on an analysis of operating conditions, the results of periodic structural integrity inspections, and the extrapolation of time dependencies between the parameters of the technical condition of the object (characteristics of the processes leading to fracture) to a certain critical value. When assessing the fatigue life of real structures, various fatigue curves and hypotheses of damage accumulation are used. To increase the accuracy of prediction, various criteria for damage to the object structure are used. A microcrack formed in a solid is a point source of an elastic wave [42,43]. Based on the assumptions of elastic deformation of the structural element, the energy released in connection with the formation of microcracks is related to the size of the structural element and the stress on it at the time of fracture. Part of this energy is converted into the energy of an elastic wave, which, as it approaches the surface of the material, decays depending on the frequency of the wave, its attenuation coefficient, and the distance traveled to the AE registration site. Of the total elastic waves emitted from the material, acoustic emission equipment registers only a part of those falling within a certain range limited by the upper and lower levels of amplitude, frequency, and time discrimination (according to the minimum duration of pauses) [44].

The formation of microcracks by the thermal fluctuation mechanism, taking into account the concentration criterion, can be expressed as

$$\frac{dC(t)}{dt} = \frac{C_0 - C(t)}{\tau(t)} \tag{3}$$

where C_0 is the maximum possible value of the microcrack concentration for a given specimen; $C(t)$ is the concentration of microcracks at time t; and τ is the waiting time for the thermal fluctuation formation of a microcrack or an elementary crack jump.

Since real bodies have structural heterogeneity, the waiting time for microcrack formation will vary and generally be stochastic. To describe the time to microcrack formation, a formula similar to the thermal activated fracture formula is used, where the parameter γ is

structure-sensitive. Therefore, by introducing a distribution γ by structural elements at this stage of destruction, the rate of increase in the concentration of microfractures is

$$C(t) = C_0 \int_{\omega}^{\omega+\Delta\omega} \Psi(\omega) \left(1 - exp \left[- \int_0^{t_f} \frac{dt}{\tau(\omega(t))} \right] \right) d\omega \quad (4)$$

where $\omega = {}^{\gamma\sigma}/_{kT}$ is a structurally sensitive parameter; $\Psi(\omega)$ is a function of the distribution density of the parameter ω; and $\Delta\omega$ is the confidence interval of the spread of values of the structural parameter. The type of function $\Psi(\omega)$ depends on the stresses and structural heterogeneity of the specimen.

AE control is influenced by a number of factors that interfere with the identification of AE sources and the isolation of the parameters of the fracture process, which requires a metrological parameter that relates the number of AE pulses and the number of fractured structural elements formed during the rupture of atomic bonds at the tips of microcracks. For this purpose, the acoustic emission coefficient k_{AE} is introduced, characterized as an acoustic active volume.

$$k_{AE} = V \iiint_{\Delta t, f, u} \Phi(\Delta t, f, u) du dt d\Delta t \quad (5)$$

where V is the volume of material subject to control (macro level) and $\Phi(\Delta t, f, u)$ is a function of the distribution density of AE signals over the duration of pauses between signals Δt, frequency f, and amplitude u. The meaning of the integral of this formula is the probability that the recorded signals fall within the range of the corresponding AE parameters.

When conducting AE tests correctly, the concentration of accumulated microcracks $C(t)$ is proportional to the primary AE parameter, such as the number $N_{\sum AE}$ of discrete AE pulses, the total count N, and the total amplitude or energy of AE. These parameters can act as $\xi(t)$, which carries information about the number of destroyed structural elements in the model.

$$\xi(t) = k_{AE} C_0 \int_{\omega_0}^{\omega_0+\Delta\omega} \Psi(\omega) \left[1 - exp \left[- \int_0^t \frac{d\bar{t}}{\theta\left(U_0, \omega(\bar{t})\right)} \right] \right] d\omega \quad (6)$$

The general equation for the time dependence of the cumulative AE parameters as damage characteristics can be written as

$$N_{AE}(t) = k_{AE} C_0 \int_{\omega_0}^{\omega_0+\Delta\omega} \Psi(\omega) \left[1 - exp \left[- \int_0^t \frac{d\bar{t}}{\theta\left(U_0, \omega(\bar{t})\right)} \right] \right] d\omega \quad (7)$$

Equation (7) is a model of time dependencies of cumulative AE parameters, which is recorded during the accumulation of damage at the stage of the fine-grained destruction of any large-scale level in conditions of heterogeneity of the structural state of the material of the object of control. The information obtained from this stage allows us to determine the parameters of the thermal activation strength equations and estimate the remaining fatigue life.

The registration of the AE parameters during the test makes it possible to distinguish two kinetic stages of the fine fracture stage, namely heterogeneous, characterized by AE instability, and homogeneous, more informative in terms of strength and having a stable rate of "fracture" of structural elements. In other words, for the stages of destruction, where the structure near the active defective region remains constant ($\gamma \approx const$)), the kinetics of damage accumulation by the thermofluctation mechanism can be described using an

individual set of kinetic parameters. The time dependence of the number of AE pulses, as a special case of the parameter $\xi(t)$, at the specified stage of homogeneous destruction in accordance with model (7) is expressed as

$$N_{\sum \text{однородн.}}(t) = \frac{k_{AE} C_0 KT exp\left[\frac{\gamma\dot{\sigma}t - U_0}{KT}\right]}{\gamma\dot{\sigma}\tau_0} \quad (8)$$

After mathematical transformation in the form of logarithmization and differentiation according to the characteristic of the material state or the test course, a number of concentration kinetic strength indicators follow from the multilevel model:

$$X_{AE} = \frac{dln\xi}{dt} = \frac{\gamma\dot{\sigma}}{KT} \quad (9)$$

$$Y_{AE} = \frac{dln\xi}{d\sigma} = \frac{\gamma}{KT} \quad (10)$$

$$W_{AE} = \frac{dln\xi}{dK_n} = \frac{\gamma\sigma}{KT} \quad (11)$$

where K_n is the loading factor equal to the ratio of the test loading to the operational load.

The above parameters make it possible to identify damage accumulation zones with characteristic kinetic parameters on the curves of cumulative AE parameters. Having information about the critical concentration of discontinuities corresponding to the transition to avalanche-like destruction, it is possible to predict the values of the remaining fatigue life of equipment.

2.3. Fatigue Life Estimation Model

The accumulation of damage, as a time parameter, is expressed in the well-known Bailey criterion, the applicability of which in the theory of thermal fluctuation destruction was confirmed in [34]. This criterion is expressed using the integral expression [45].

$$\int_0^{t_f} \frac{dt}{\tau(\sigma)} = \int_0^{t_f} \frac{dt}{\tau_0 e^{\left(\frac{U_0 - \gamma\sigma(t)}{kT}\right)}} = 1 \quad (12)$$

This criterion should be modified to take into account the concentration criterion. In this case, this integral expression corresponds to Equation (16). To predict fatigue life, it is necessary to know the parameters U_0 and γ. For a series of similar specimens and a number of materials, U_0 is an approximately constant value, and γ is a variable characterizing the individual defective structure of an individual specimen or object. Hence, U_0 can be found once, and the fatigue life calculation boils down to determining a parameter γ. The value of the latter can be found from the kinetics of the cracking process by measuring the angle of inclination of the graph $C(t)$ in semi-logarithmic coordinates under dynamic loading.

$$\frac{d\ln C}{dt} = \frac{\gamma\dot{\sigma}}{kT} \quad (13)$$

The kinetics of microcracking can be studied using some means of physical destructive and non-destructive testing, including AE. There are various modes of loading objects in which it is necessary to determine their time before destruction. To estimate fatigue life, it is necessary to transform the Zhurkov equation, taking into account the sinusoidal

dynamic mode of stress (Figure 5) and temperature changes in which the dependences of these parameters are written as

$$\sigma(t) = \overline{\sigma} + \hat{\sigma}\cos(\omega_1 t) \tag{14}$$

$$T(t) = \overline{T} + \hat{T}\cos(\omega_2 t) \tag{15}$$

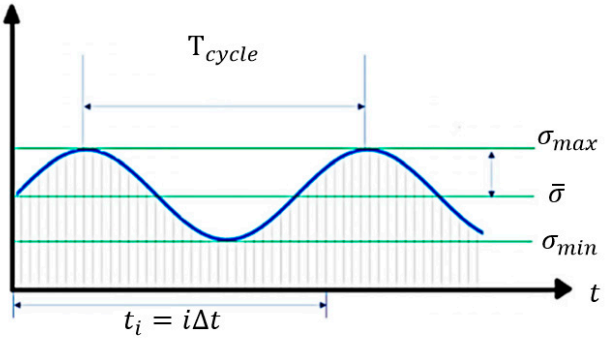

Figure 5. Cycle scheme during fatigue loading.

Similar transformations are presented in a number of articles [25–28].

Taking into account the Bailey criterion, the crack concentration criterion, and the stress change ratios in accordance with Equation (14) for cyclic loading, we obtain

$$C^* = C_0 \int_0^{t_f} \frac{dt}{\tau_0 e^{\frac{U_0 - \gamma(\overline{\sigma} + \hat{\sigma}\cos(\omega_1 t))}{k(\overline{T} + \hat{T}\cos(\omega_2 t))}}} = C_0 \int_0^{t_f} \frac{dt}{\tau_0 e^{\frac{U_0 - \gamma\overline{\sigma}(1 + (\hat{\sigma}/\overline{\sigma})\cos(\omega_1 t))}{k\overline{T}(1 + (\hat{T}/\overline{T})\cos(\omega_2 t))}}} \tag{16}$$

The critical concentration of microcracks (or decompaction) occurs, after which the short-term development of a macrofracture begins, and the total concentration is related to the ratio $C^*/C_0 \approx 0.01$ [46–48]. Then, Equation (16) can be rewritten as

$$\int_0^{t_f} \frac{dt}{\tau_0 e^{\frac{U_0}{k\overline{T}(1 + (\hat{T}/\overline{T})\cos(\omega_2 t))} - \frac{\gamma\overline{\sigma}}{k\overline{T}(1 + (\hat{T}/\overline{T})\cos(\omega_2 t))} - \frac{\gamma\overline{\sigma}(\hat{\sigma}/\overline{\sigma})\cos(\omega_1 t))}{k\overline{T}(1 + (\hat{T}/\overline{T})\cos(\omega_2 t))}}} = 0.01 \tag{17}$$

This is under conditions when $\hat{T} \ll \overline{T} \rightarrow \left(1 + \left(\hat{T}/\overline{T}\right)cos(\omega_2 t)\right) \approx 1$. This approximation is justified by the fact that $\hat{T}$ is a relatively small perturbation of $\overline{T}$. Then,

$$\frac{1}{\tau_0 e^{\frac{U_0 - \gamma\overline{\sigma}}{k\overline{T}}}} \int_0^{t_f} \frac{dt}{e^{-\left(\frac{\gamma\overline{\sigma}}{k\overline{T}}\right)\frac{(\hat{\sigma}/\overline{\sigma})\cos(\omega_1 t))}{(1 + (\hat{T}/\overline{T})\cos(\omega_2 t))}}} = 0.01 \tag{18}$$

When decomposing the exponential function into a first-order Taylor series for conditions $x \ll 1$, we obtain $e^x \approx 1 + x$. Then,

$$1 + \left(\hat{T}/\overline{T}\right)\cos(\omega_2 t) \approx e^{(\hat{T}/\overline{T})\cos(\omega_2 t)} \tag{19}$$

Substituting the denominator in the integral into the original expression becomes equal to

$$e^{-\left(\frac{\gamma\overline{\sigma}}{k\overline{T}}\right)\frac{(\hat{\sigma}/\overline{\sigma})\cos(\omega_1 t))}{(1 + (\hat{T}/\overline{T})\cos(\omega_2 t))}} \approx e^{-\left(\frac{\gamma\overline{\sigma}}{k\overline{T}}\right)\frac{(\hat{\sigma}/\overline{\sigma})\cos(\omega_1 t))}{e^{(\hat{T}/\overline{T})\cos(\omega_2 t)}}} \tag{20}$$

Considering that $\hat{T} \ll \overline{T}$

$$e^{(\hat{T}/\overline{T})\cos(\omega_2 t)} \approx 1 \tag{21}$$

Equation (18) can be modified to the form

$$\frac{1}{\tau_0 e^{\frac{U_0-\gamma\overline{\sigma}}{kT}}} \int_0^{t_f} \frac{dt}{e^{-(\frac{\gamma\overline{\sigma}\hat{\sigma}}{k\overline{T}\overline{\sigma}})\cos(\omega_1 t)} e^{-(\frac{\gamma\overline{\sigma}\hat{T}}{k\overline{T}\overline{T}})\cos(\omega_2 t)}} = 0.01 \tag{22}$$

However, Equation (22) cannot be integrated directly. Thus, the equation should be transformed using the condition of the Cauchy–Schwarz inequality.

$$\int_a^b f(x)g(x)dx \le \left[\int_a^b f^2(x)dx \int_a^b g^2(x)dx\right]^{0.5} \tag{23}$$

In this condition, the left and right sides are equal only if $e^{(\frac{\gamma\overline{\sigma}\hat{\sigma}}{k\overline{T}\overline{\sigma}}\cos\omega_1 t)}$ and $e^{(\frac{\gamma\overline{\sigma}\hat{T}}{k\overline{T}\overline{T}}\cos\omega_2 t)}$ are proportional expressions. Then, we obtain

$$\frac{1}{\tau_0 e^{(\frac{U_0-\gamma\overline{\sigma}}{kT})}} \int_0^{t_f} e^{(\frac{\gamma\overline{\sigma}\hat{\sigma}}{k\overline{T}\overline{\sigma}}\cos\omega_1 t)} e^{(\frac{\gamma\overline{\sigma}\hat{T}}{k\overline{T}\overline{T}}\cos\omega_2 t)} dt \le \frac{1}{\tau_0 e^{(\frac{U_0-\gamma\overline{\sigma}}{kT})}} \left[\int_0^{t_f} \left(e^{(\frac{\gamma\overline{\sigma}\hat{\sigma}}{k\overline{T}\overline{\sigma}}\cos\omega_1 t)}\right)^2 dt \int_0^{t_f} \left(e^{(\frac{\gamma\overline{\sigma}\hat{T}}{k\overline{T}\overline{T}}\cos\omega_2 t)}\right)^2 dt\right]^{0.5} = 0.01 \tag{24}$$

The integral terms of the exponential function with respect to dt in the right-hand side of Equation (24) can be simplified by using a modified Bessel function. The modified Bessel function of the first kind $I_0(\alpha)$ is a function that is defined for all complex values of α. This function is used to find solutions to differential equations in various scientific and engineering disciplines, especially in mechanics. We introduce a modified Bessel function $I_0(\alpha)$ with the following characteristics:

$$\begin{aligned} I_0(0) &= 1, \\ I_0(x) &= e^x/\sqrt{2\pi x}, \\ I_0(2x) &= e^{2x}/\sqrt{2\pi 2x} \quad = I_0^2(x)\sqrt{\pi x} \end{aligned} \tag{25}$$

$I_0(x)$ and $I_0(2x)$ are obtained by Hankel decompositions based on asymptotic forms for a large value of the argument x [49]. A more detailed derivation of the Bessel function of the first kind of order zero is presented in Appendix A. The integral of an exponential function containing a sinusoidal function in the exponent is related to the Bessel function as

$$\int_0^{t_f} e^{(\frac{\gamma\overline{\sigma}\hat{\sigma}}{k\overline{T}\overline{\sigma}}\cos\omega_1 t)} dt = t_f I_0\left(\frac{\gamma\overline{\sigma}}{k\overline{T}}\frac{\hat{\sigma}}{\overline{\sigma}}\right) \tag{26}$$

$$\int_0^{t_f} e^{(\frac{\gamma\overline{\sigma}\hat{T}}{k\overline{T}\overline{T}}\cos\omega_2 t)} dt = t_f I_0\left(\frac{\gamma\overline{\sigma}}{k\overline{T}}\frac{\hat{T}}{\overline{T}}\right), \tag{27}$$

Assuming that $\frac{\gamma\overline{\sigma}}{k\overline{T}} \gg 0$, a modified Bessel function of the first kind of order zero gives the expression

$$I_0\left(\frac{\gamma\overline{\sigma}}{k\overline{T}}\right) \cong \frac{\exp\left(\frac{\gamma\overline{\sigma}}{k\overline{T}}\right)}{\sqrt{2\pi\left(\frac{\gamma\overline{\sigma}}{k\overline{T}}\right)}} \tag{28}$$

Using expressions (27) and (28), we transform the right-hand side of Equation (24).

$$0.01 \le \frac{1}{\tau_0 e^{\left(\frac{U_0-\gamma\overline{\sigma}}{kT}\right)}} t_f \left[I_0\left(2\frac{\gamma\overline{\sigma}}{k\overline{T}}\frac{\hat{\sigma}}{\overline{\sigma}}\right) I_0\left(2\frac{\gamma\overline{\sigma}}{k\overline{T}}\frac{\hat{T}}{\overline{T}}\right)\right]^{0.5} \tag{29}$$

Solving with respect to the time to destruction and neglecting the temperature change, after substituting Equation (29), we obtain

$$t_f \ge 0.01 \frac{\tau_0 e^{\left(\frac{U_0-\gamma\overline{\sigma}}{kT}\right)}}{\left[I_0\left(2\frac{\gamma\overline{\sigma}}{k\overline{T}}\frac{\hat{\sigma}}{\overline{\sigma}}\right) I_0\left(2\frac{\gamma\overline{\sigma}}{k\overline{T}}\frac{\hat{T}}{\overline{T}}\right)\right]^{0.5}} \tag{30}$$

Since $T \ll T$ we obtain

$$t_f \ge 0.01 \frac{\tau_0 e^{\left(\frac{U_0-\gamma\overline{\sigma}}{kT}\right)}}{\left[I_0\left(2\frac{\gamma\overline{\sigma}}{k\overline{T}}\frac{\hat{\sigma}}{\overline{\sigma}}\right)\right]^{0.5}} \tag{31}$$

Let us rewrite the equation as

$$t_f = 0.01\tau_0 \sqrt{2\pi\frac{\gamma\hat{\sigma}}{k\overline{T}}} \cdot e^{\left(\frac{U_0-\gamma(\overline{\sigma}+\hat{\sigma})}{kT}\right)} \tag{32}$$

The equations for determining the number of cycles before fracture are obtained, bearing in mind the relationship between the durability of the body and the frequency of cyclic loading.

$$N_f = \tau_f \cdot f \tag{33}$$

Then, Equation (32) takes the following form:

$$N_f = 0.01 f \tau_0 \sqrt{2\pi\frac{\gamma\hat{\sigma}}{k\overline{T}}} \cdot e^{\left(\frac{U_0-\gamma(\overline{\sigma}+\hat{\sigma})}{kT}\right)} \tag{34}$$

3. Results

In accordance with the experimental methodology described above, mechanical tests were carried out with the recording of acoustic emission signals (Figure 6).



Figure 6. A-Line work screen for processing AE signals during Specimen VII tests. Red color—1 channel; green color—2 channel.

The task was to determine the concentration and kinetic parameters obtained during static tests for a single destructive load. Information about the structural and strength heterogeneity embedded in the desired parameters X_{AE} and Y_{AE} should be used in the second part of calculations aimed at determining the residual fatigue life, since both proposed models are based on the thermofluctuational nature of the fracture. Single destructive tests were carried out on specimens with different operating times and initial specimens with stress control, since this type of loading is most similar to real hydraulic and pneumatic tests of vessels and pipelines. Figure 7 shows the test results; the time dependence of the total AE count and stress change over time.

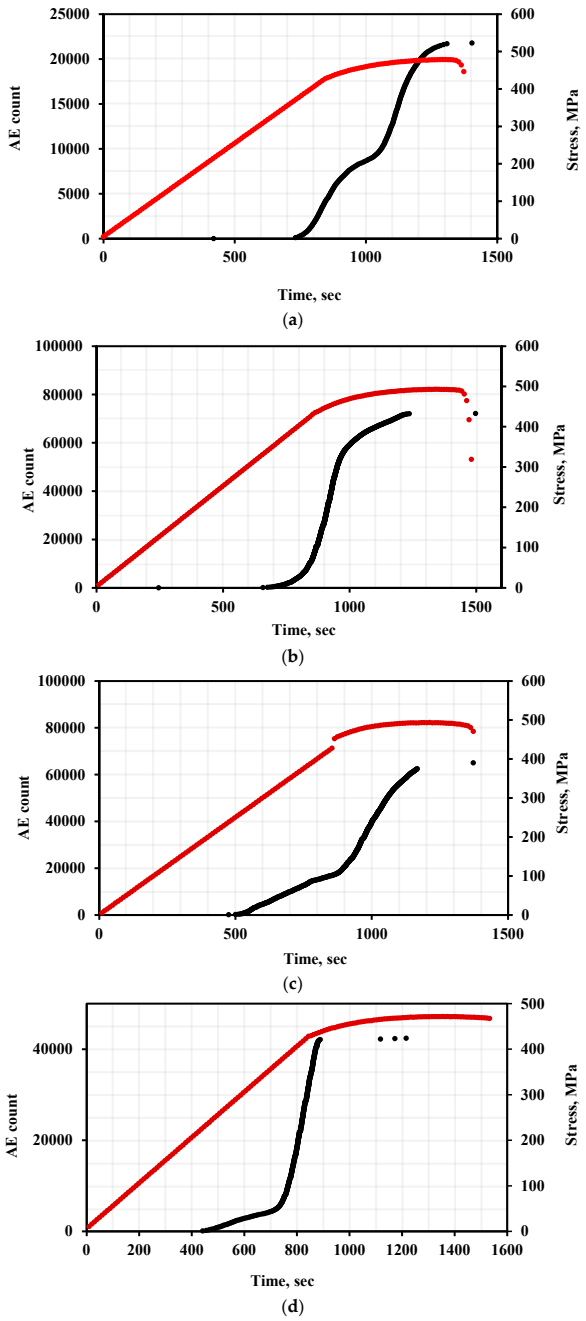

Figure 7. Time dependences of the cumulative AE count (black points) and stress changes (red points) during single tensile tests after various degrees of operation at 213 K: (**a**) without operation (Specimen I); (**b**) $N_i/N_f = 0.3$ at $\sigma_{max} = 460$ MPa (Specimen VI); (**c**) $N_i/N_f = 0.5$ at $\sigma_{max} = 480$ MPa (Specimen VII); and (**d**) $N_i/N_f = 0.7$ at $\sigma_{max} = 500$ MPa (Specimen VIII).

Analyzing the data in Figure 7, it can be seen that the greatest AE activity corresponded to the period covering the end of the elastic deformation section and the beginning of the elastoplastic deformation. On all dependences, these time intervals corresponded to the exponential nature of the dependence of the cumulative AE count. It follows that at these stages, the processes of damage accumulation are most active. This assumption is confirmed by the results of observations of the accumulation of microcracks during deformation. A network of microcracks is formed in the zone of intermediate stresses in the upper part of the elastic region and during elastoplastic deformation during the development of a system of slip bands and the overcoming of energy barriers by dislocation clusters.

The stage of homogeneous fracture is associated with the accumulation of microcracks in the area in front of the stress concentrator, namely the crack. If the specimen does not have a pronounced concentrator, the stage of homogeneous fracture takes approximately 60% of the first stage of fracture. Otherwise, when a concentrator has already formed during the coalescence of pores and the growth of microcracks, the stage of homogeneous fracture lasts for a shorter period.

The transition to homogeneous fracture was analyzed in [50] in terms of the influence of structural heterogeneity during the clustering process. The accelerated growth of the fracture source, associated with the overstresses it creates on the boundary elements, is hindered by the need to fracture an increasingly stronger (with a smaller value of γ) microstructure, which leads to the delocalization of the fracture and expansion of the area of action of the statistical mechanism of microcrack coalescence. This is evidenced by the jump-like nature of damage accumulation (AE signals) at the initial stage of loading.

Three criteria are used to identify the stage of homogeneous fracture using AE diagnostics as follows:

- Kinetic: approximation of the time dependence of cumulative AE parameters for homogeneous fracture (determination of the linear section of the AE dependence in semi-logarithmic coordinates).
- Statistical: accounting for the stabilization of the values of amplitude, frequency, and pause distributions of AE during the time interval of homogeneous fracture.
- Elastoplastic deformation criterion: the accumulation of microdamage corresponding to homogeneous fracture occurs before the beginning of structural rearrangements during plastic deformation in the upper region of elastic and the beginning of elastoplastic deformation.

The first—the linear section of the logarithm of the cumulative count—is marked by lines in Figure 8. The third can be seen in Figure 7, since the exponential dependence of the cumulative count corresponds to the end of the elastic section or the beginning of the elastoplastic section on the stress–strain diagram. In the case of a complete set of AE data, it is necessary to use a statistical feature that includes information about the time intervals between AE signals, amplitude variations, AE activity, etc. (see Figure 9).

Using Equation (34) according to the data in Figure 8, the parameters X_{AE} and Y_{AE}, the activation energy of fracture, and the structural parameter γ were calculated. The calculations took into account the loading rate, which was 0.5 MPa/sec for the elastic loading stage and approximately 0.15 MPa/sec for the elastoplastic fracture stage.

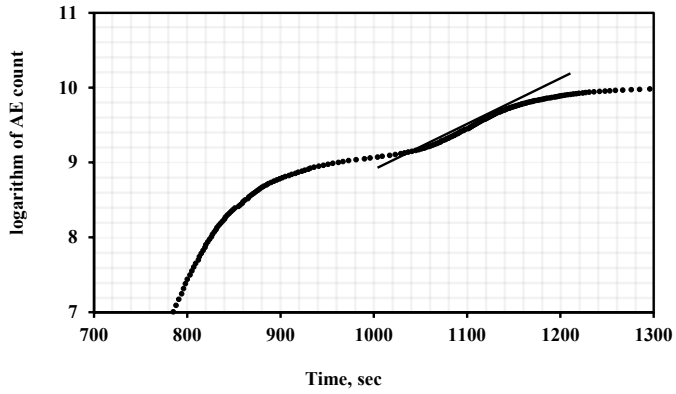

(**a**)

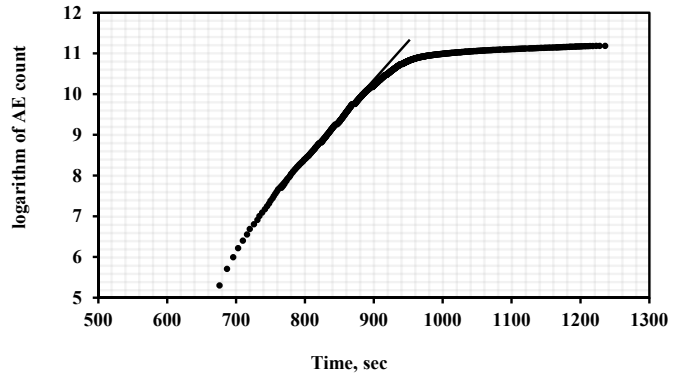

(**b**)

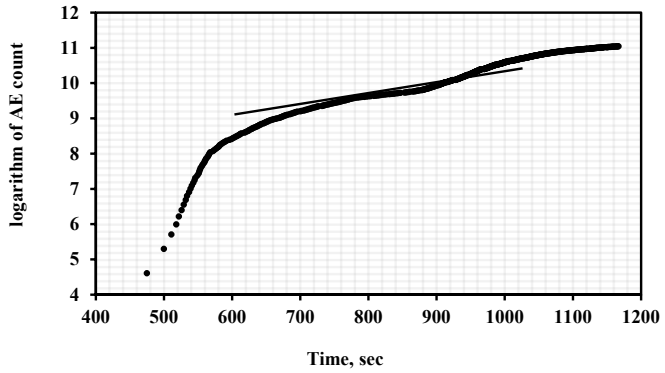

(**c**)

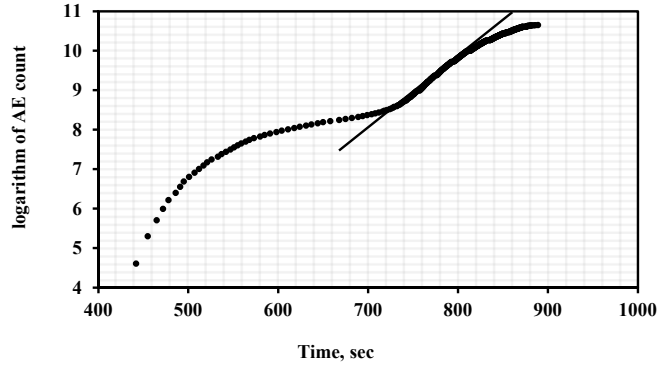

(**d**)

Figure 8. Time dependence of the logarithm of the cumulative AE count: (**a**) without pre-fatigue (Specimen I); (**b**) $N_i/N_f = 0.3$ at $\sigma_{max} = 460$ MPa (Specimen VI); (**c**) $N_i/N_f = 0.5$ at $\sigma_{max} = 480$ MPa (Specimen VII); and (**d**) $N_i/N_f = 0.7$ at $\sigma_{max} = 500$ MPa (Specimen VIII).

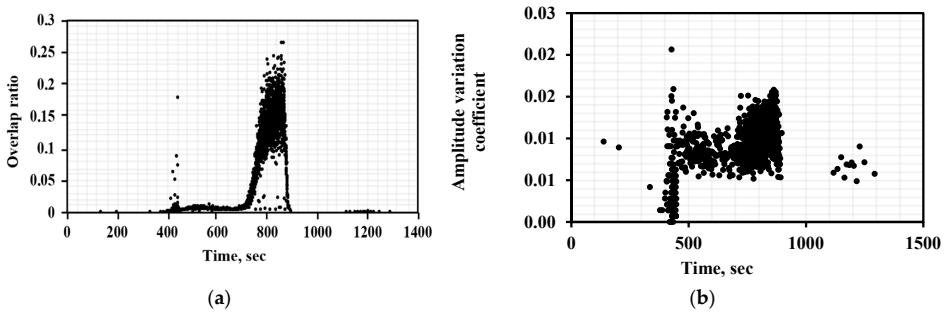

Figure 9. AE features for determining the start and end times of the uniform fracture stage for specimen VII ($N_i/N_f = 0.7$ at $\sigma_{max} = 500$ MPa): (**a**) time dependence of the signal overlap coefficient; (**b**) time dependence of the amplitude variation coefficient.

Furthermore, using the obtained values of the structural parameter included in Y_{AE}, the values of the initial activation energy U_0 and the loading frequency f, the fatigue life was determined using Equation (34). The image of the specimens after the tests is shown in Figure 10. The results are summarized in Figure 11a, which shows the low-cycle branch of the fatigue curve according to calculated and experimental values, as well as points corresponding to partial accumulation. The discrepancy between the calculated and experimental values may be due to the insufficient consideration of structural changes during cyclic deformation in the initial and final parts of the fatigue life associated with the stabilization of the structure and the formation of a main crack, respectively. Because of this, the change in the γ parameter was not taken into account during the calculation of the number of cycles before destruction As can be seen from Table 3, for specimens VI and VII, the calculation error was 9.9% and 22%, respectively; for specimen VIII, it exceeded 100%. However, in absolute values, this corresponded to 6531, 4372, and 6963 cycles, respectively, which allows for establishing an adequate value for the lower limit of fatigue life. This expression allows for taking into account the test temperature, and as can be seen from Figure 11b, lowering the temperature increased the fatigue life. The indicated figure shows the results of fatigue tests of the same St-3sp steel according to the data of Strizhalo [51]. The points corresponding to quasi-static failure are marked with unpainted markers, and the fully filled-in markers correspond to fatigue failure. It can be noted that as the temperature decreases, the fatigue failure region expands to a region of higher stresses. For comparison with our data, we used the data obtained by Strizhalo for the same grade of steel in a similar temperature range. However, even for the same steel grade, the scatter in fatigue life can reach one order of magnitude, which indicates the importance of taking into account the structural features of the steel.

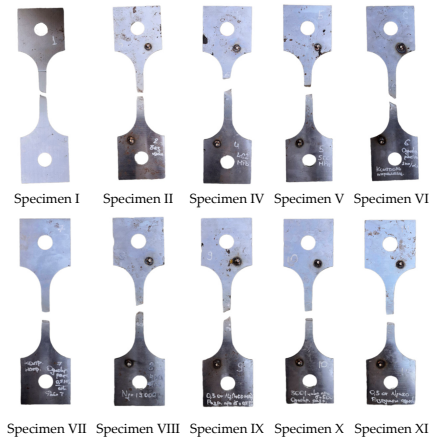

Figure 10. Photo of specimens that underwent static tensile and fatigue tests: specimens I, II, and specimens IV–XI.

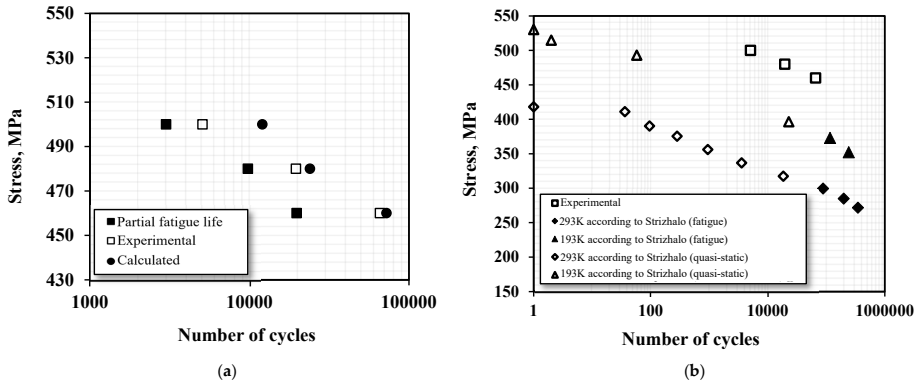

Figure 11. Results of fatigue life calculations based on low-temperature AE testing: (**a**) calculated and experimental fatigue life values; (**b**) fatigue curve of St-3 steel at low temperatures for similar specimens according to Strizhalo [51].

As an example of implementing the method for finding the parameters of the durability equation using acoustic emission and calculating the fatigue life, we will also use the data from Botvina et al. [52–54] and present a series of tests, the results of which were used to calculate the parameters X_{AE} and Y_{AE}. Tensile tests were conducted after three levels of fatigue accumulation, namely 0.3, 0.5, and 0.7, as well as in the initial state. The time dependencies of the cumulative AE count and its logarithm are presented in Figure 12 according to the data from references [52–56]. The frequency of the preliminary cyclic loading was 30 Hz with a stress ratio R = 0.1 at 390, 330, 460, and 800 MPa, respectively. Fatigue tests were carried out in accordance with BS EN ISO 12135 and GOST 25.502 in all three experiments. Before the tensile tests, fatigue curves were plotted for the given material, which were used to determine the approximate fatigue life. Several specimens were tested at the very beginning to determine the basic mechanical properties.

Table 3. Results of fatigue life calculation based on low-temperature AE tests.

Specimen Number	Degree of Service Life	Maximum Stress, MPa	Stress Amplitude, MPa	Mean Stress, MPa	Fracture Stress, MPa	Loading Rate, MPa/sec	X_{AE}, sec^{-1}
Specimen I	Without pre-fatigue	-	-	-	478	0.152	0.005873
Specimen VI	0.3	486	229	237	493	0.5	0.020355
Specimen VII	0.5	466	240	246	493	0.16	0.006613
Specimen VIII	0.7	505.5	249	257	471	0.5	0.02069

Specimen Number	Y_{AE}, MPa^{-1}	u_{AE}, $J/mole$	u_{0fat}, $J/mole$	γ, $\frac{J}{mole \cdot MPa}$	Calculated Number of Cycles to Fracture	Actual Fatigue Life	Preliminary Work Cycles
Specimen I	0.0386	146,477					
Specimen VI	0.0407	145,143		1.67×10^{-22}	72,412	65,881	19,765
Specimen VII	0.0413	150,904	121,936	1.69×10^{-22}	23,954	19,582	9791
Specimen VIII	0.0414	148,139		1.70×10^{-22}	12,044	5081	3004

Based on the results of AE diagnostics, sections of homogeneous fracture corresponding to the zone of elastoplastic deformations were identified as linear sections of the logarithm of the cumulative AE count. For specimens made of 15Kh2GMF steel, data are presented for the initial state (without fatigue accumulation), after an accumulation of 0.7 of fatigue life, and for a tensile test of a standard specimen with different dimensions. Similar results of a static single fracture test of 09G2S steel after accumulation of 0.2, 0.3, 0.5, 0.7, and 0.9 of the total life were also used [57].

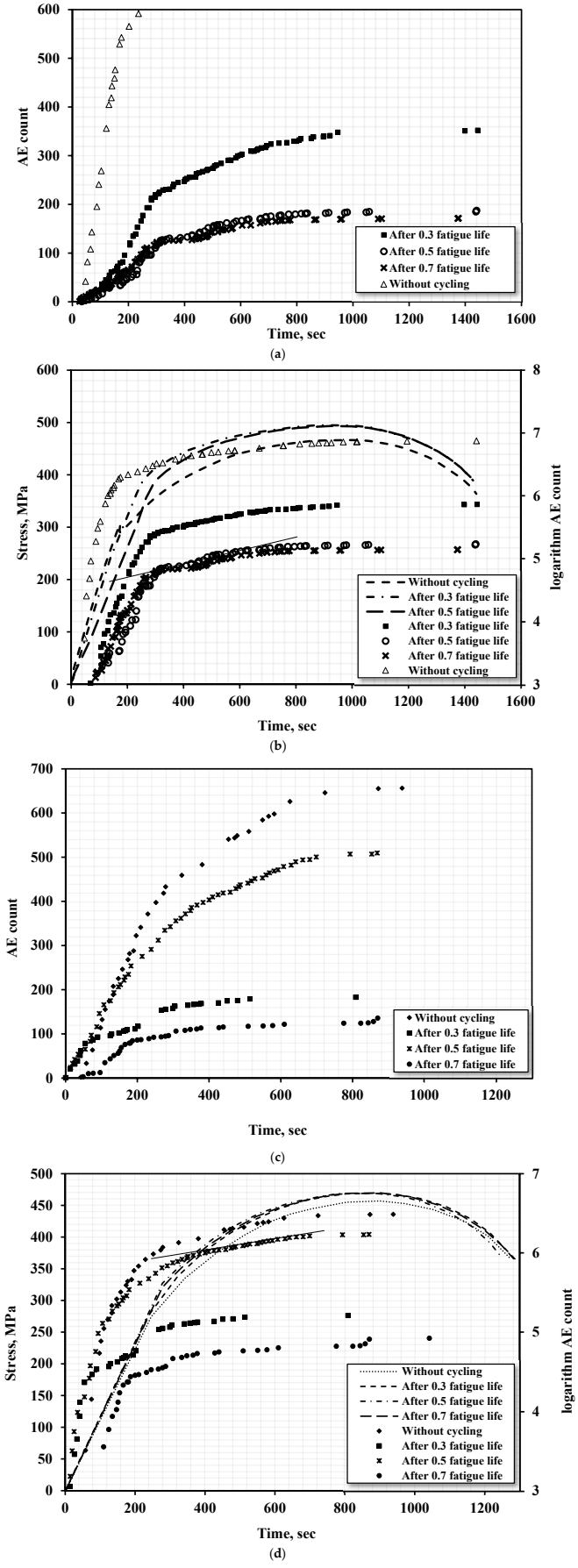

Figure 12. *Cont*.

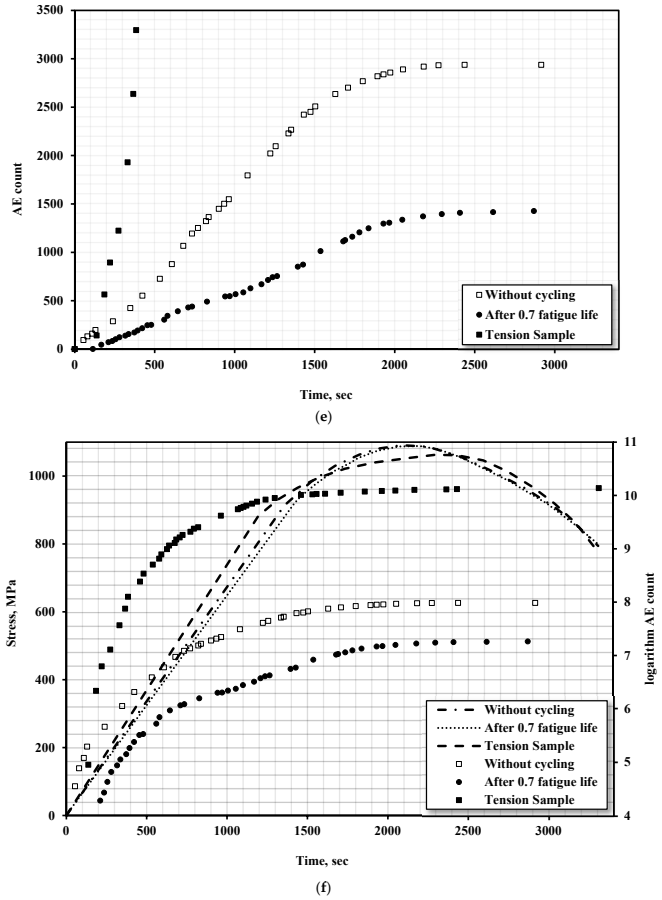

Figure 12. Results of acoustic emission tests for single static fracture of standard specimens after various levels of fatigue accumulation: (**a**) time dependencies of the cumulative AE count for specimens after an accumulation of 0.3, 0.5, and 0.7 of the life and in the initial state during static tests and (**b**) time dependencies of the logarithm of the cumulative AE count and stress–strain curves (steel 20) [58]; (**c**) time dependencies of the cumulative AE count for specimens after an accumulation of 0.3, 0.5, and 0.7 of the life and in the initial state during static tests and (**d**) time dependencies of the logarithm of the cumulative AE count and stress–strain curves (low-carbon steel 20) [55]; (**e**) time dependencies of the cumulative AE count for specimens after an accumulation of 0.3, 0.5, and 0.7 of the life, in the initial state and a tensile specimen during static tests and (**f**) time dependencies of the logarithm of the cumulative AE count and stress–strain curves (steel 15Kh2GMF) [53].

The calculated values of the parameters X_{AE} and Y_{AE}, as well as the structural parameter γ and the number of cycles to fracture at an amplitude equal to that at which the preliminary loading was performed, are summarized in Table 4.

Table 4. Results of fatigue life calculation using AE kinetic parameters according to data from various authors.

Material	Specimen Part of Fatigue Life	X_{AE}, c^{-1}	Y_{AE}, MPa^{-1}	γ, $\frac{J}{mole \cdot MPa}$	U_0, $\frac{J}{mole}$	σ_{max}, MPa	N_f, Cycles
Steel 20 [52]	Without pre-fatigue	0.00122	0.00464	11.29	108,456	390	245,639
	0.3	0.00095	0.00543	13.21	110,004		368,865
	0.5	0.00094	0.00439	10.69	108,793		302,112
	0.7	0.00085	0.00399	9.71	108,544		303,987

Table 4. *Cont.*

Material	Specimen Part of Fatigue Life	X_{AE}, c^{-1}	Y_{AE}, MPa^{-1}	γ, $\frac{J}{mole \cdot MPa}$	U_0, $\frac{J}{mole}$	σ_{max}, MPa	N_f, Cycles
Steel 20 [55]	Without pre-fatigue	0.001063	0.00775	18.873	111,833	330	552,452
	0.3	0.00292	0.02126	51.765	125,029		2,393,607
	0.5	0.00084	0.00612	14.913	110,791		547,412
	0.7	0.00198	0.01442	35.121	118,203		677,940
15Kh2GMF [53]	Without pre-fatigue	0.00091	0.00136	3.304	107,182	800	23,230,799
	0.7	0.00099	0.00153	3.726	107,431		23,784,674
	Tensile specimen	0.00115	0.001556	3.789	107,047		20,064,926
12Kh18N9TL [56]	Without pre-fatigue	0.000382	0.002085	5.077	108,796	460	480,758
	0.3	0.000308	0.001682	4.097	108,720		503,830
	0.5	0.00028	0.001528	3.721	108,725		516,559
	0.7	0.000356	0.001939	4.723	108,756		487,706
12Kh18N9TL (after operation) [56]	Without pre-fatigue	0.00023	0.001061	2.583	108,487	460	483,764
	0.3	0.000271	0.001249	3.041	108,574		499,030
	0.5	0.000181	0.000832	2.026	108,894		562,524
	0.7	0.000351	0.001617	3.938	108,546		473,814

Points corresponding to the fatigue life of the specimens are marked on the fatigue curves for these specimens. The fatigue curves and the marked calculated life values are shown in Figure 13. The least squares method was used to determine the dependence of the number of cycles before failure on the applied stress.

The indicated figures show the plotted parts of the fatigue curves corresponding to low-cycle fatigue. It is difficult to judge the specific value of the fatigue limit, since only high-stress data are available. The highest values of the number of cycles before destruction obtained during the experiment lie in the area of low-cycle fatigue. To describe the accumulation of damage during homogeneous fine-dispersed fracture at the stage of elastic deformation, a micromechanical model of the form of Equation (7) is used. The program compiled to estimate the time to fracture based on AE data uses the homogeneous fracture stage for approximation. Structural heterogeneity and non-uniformity of the stress state throughout the material volume influence the average time to fracture of the structural elements of the body [59]. The durability parameter is not the same for different elements. To account for such heterogeneity, a distribution function of the parameter γ over the structural elements was introduced. The function $\Psi(\gamma)$ has different distributions depending on the degree of heterogeneity. In this article, a bounded Weibull and log-normal distribution were used for the fracture of specimens of various structural materials.

In this work, the bounded Weibull distribution is written as

$$\Psi(\gamma) = \begin{cases} 0, \quad \lambda \in [0, q), \\ A\left(\frac{k}{\lambda}\right)\left(\frac{\gamma}{\lambda}\right)^{k-1}\exp\left(\left(-\frac{\gamma}{\lambda}\right)^{k}\right), \gamma \in [q, \infty); \end{cases}$$
$$A = \frac{1}{\int_q^\infty \left(\frac{k}{\lambda}\right)\left(\frac{\gamma}{\lambda}\right)^{k-1}\exp\left(\left(-\frac{\gamma}{\lambda}\right)^{k}\right)d\gamma} \tag{35}$$

where the distribution parameters are $k, \lambda, q.{}^{1}/_{A}$—the coefficient relating the loading in N and the stress in MPa—represents the value inverse to the cross-sectional area of the standard specimen. Log-normal distribution with parameters σ_z, μ is

$$\Psi(\gamma) = \frac{1}{\sqrt{2\pi}\sigma_z \gamma} exp\left[-\frac{(ln(\gamma) - \mu)^2}{2{\sigma_z}^2}\right] \tag{36}$$

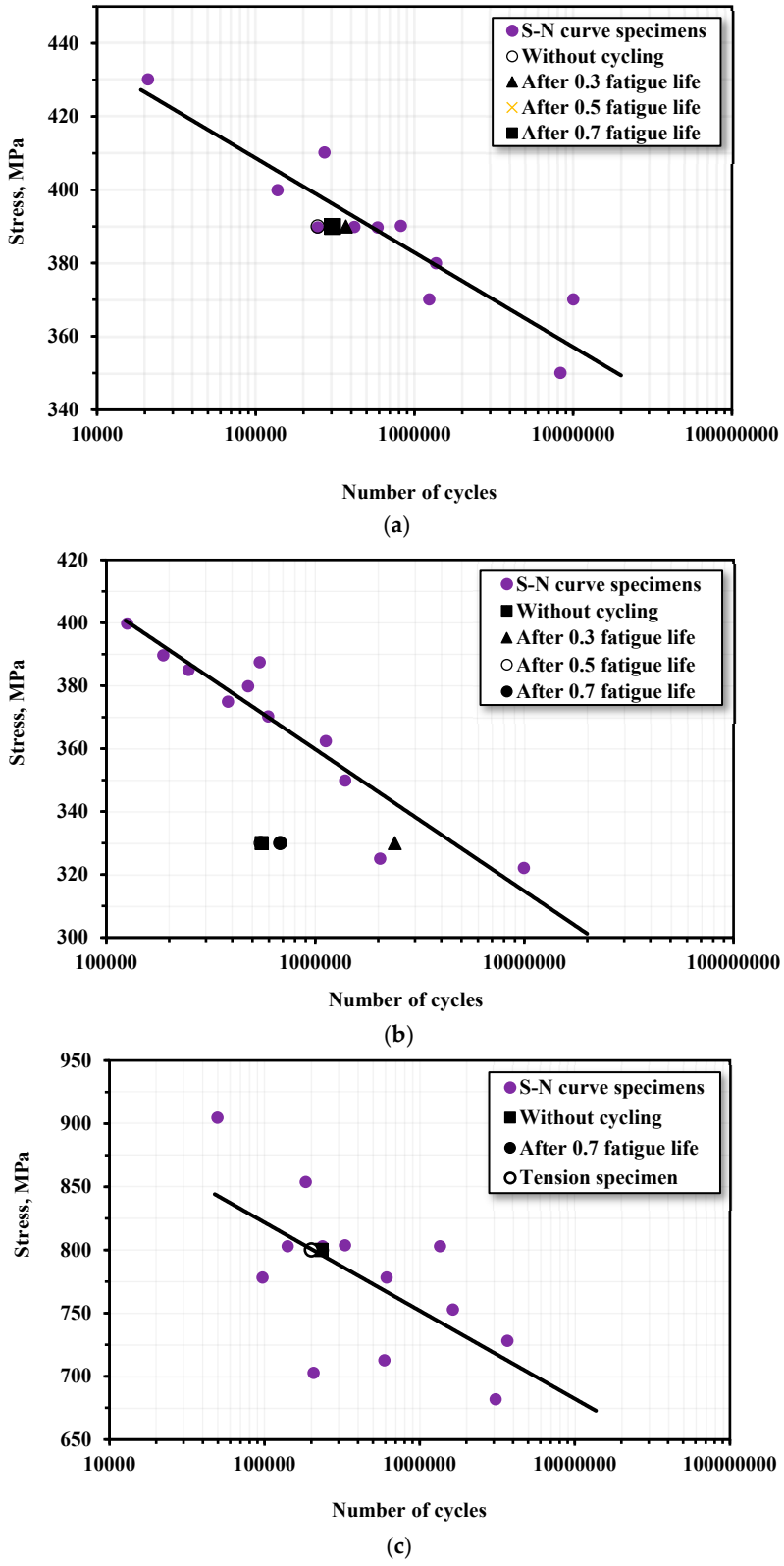

Figure 13. Fatigue curves for the experimental materials with marked points of the calculated fatigue life: (**a**) steel 20 with preliminary cycling at 390 MPa; (**b**) steel 20 with preliminary loading at 330 MPa; and (**c**) steel 15Kh2GMF with preliminary loading at 800 MPa.

As indicated, the transition to spontaneous fracture and macroscopic crack formation occurs when the number of broken structural bonds reaches $C/C_0 \approx 0.01$, which

corresponds to the difference in volume concentrations and the concentration criterion for fracture. Then, Equation (36) takes the following form:

$$\int_{\gamma_{min}}^{\gamma_{max}} \Psi(\gamma) \left[1 - exp \left[- \int_0^t \frac{d\bar{t}}{\tau_0 \exp\left(\frac{U_0 - \gamma\sigma(t)}{kT} \right)} \right] \right] d\gamma = 0.01 \quad (37)$$

Thus, an automated program for approximating the theoretical and experimental curve of the cumulative acoustic emission count can be used to assess the scatter of the structural parameter of thermofluctuation fracture. This analysis was conducted on the results of low-temperature AE tests. Using the identified stages of uniform fracture based on the three indicated features, distribution curves of the structural parameter γ were plotted, and the parameters of the log-normal and Weibull distributions were calculated (see Table 5).

Table 5. Results of numerical modeling of structural heterogeneity of specimens subjected to fatigue loading at negative temperatures.

Specimen Number	t_1	t_2	Weibull					Log-Normal			
			k	λ	q	E_A,%	E_{Tf},%	σ_z	μ	E_A,%	E_{Tf},%
VI	859	916	3	80	0	1.85	5.48	0.17	4.7	1.55	7.69
VII	891	965	3	100	0	1.93	10.04	0.22	4.7	1.52	18.09
VIII	757	799	3	95	0	2.06	4.26	0.135	4.7	1.58	0.27

In this case, it is even more clearly seen that the value of the parameter γ found using AE testing corresponds to the peak of the distribution, i.e., the array of structural volumes of the body whose strength characteristics determine the overall strength. The correspondence of the structural parameter values to the peak of the distribution is shown in Figure 14.

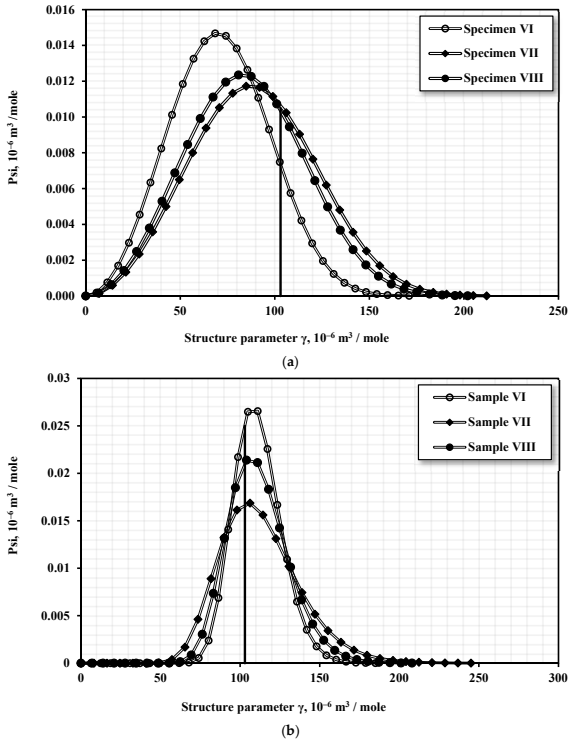

Figure 14. Distribution of the structural parameter γ during uniform fracture of specimens VI, VII, and VIII. (**a**) Weibull distribution; (**b**) log-normal distribution.

Based on the obtained distribution, the theoretical time dependence of the cumulative AE count during the uniform fracture stage was constructed and compared with experimental values. As can be seen in the example of the Weibull distribution (Figure 15), the approximation error did not exceed 2% for all specimens, and the curves closely approximate the point values of the cumulative AE count.

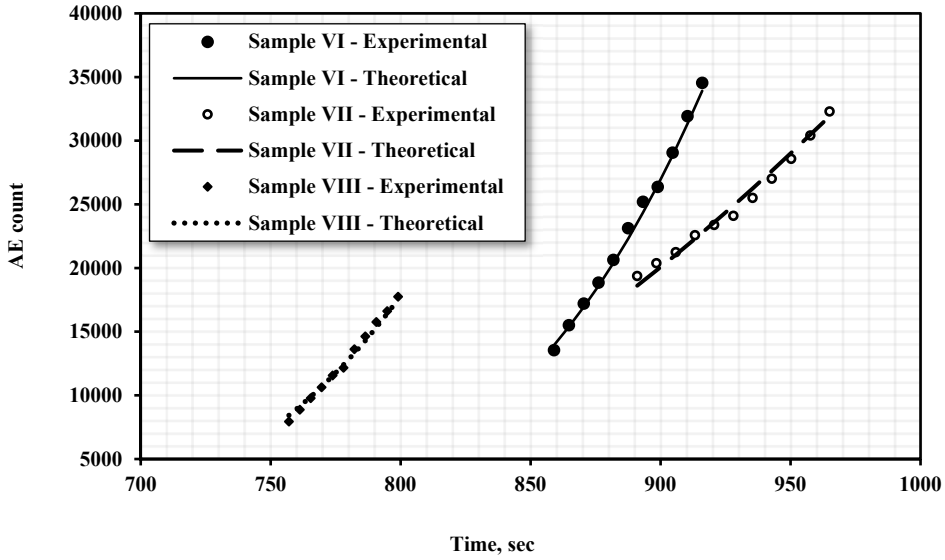

Figure 15. Comparison of experimental and calculated values of cumulative AE count based on numerical simulation data.

4. Discussion

For specimens VI and VIII, the stage of uniform fracture, characterized by the linear nature of the time dependence of the logarithm of the cumulative AE count, corresponds to the elastic deformation section; for specimen I, it is on the elastoplastic deformation stage, and for specimen VII, it is on the transition zone. At the same time, despite the difference in the stress growth rate for all specimens, which is included in Equation (9) for the parameter X_{AE}, the values of the parameter Y_{AE} remained the same (≈ 0.4) for all specimens.

This result is of great importance for calculating fatigue life. The similarity of the parameter Y_{AE} for both the initial state and for the specimens after fatigue loading indicates that the kinetics of microcrack accumulation at the elastoplastic deformation stage (in the zone of natural and artificial stress concentrators of real equipment) remains constant for most of the service life, at least from 0.3 to 0.7 of the total lifetime. In this case, the results of acoustic emission hydraulic and pneumatic tests allow for calculating the number of cycles to fracture regardless of when the test was conducted. To calculate the remaining fatigue life, in this case, it is necessary to know the history of the operational loading of the structure. Despite the small scatter of the γ parameter, the lifetime value strongly depends on other kinetic parameters. Therefore, two values of the activation energy of fracture were calculated. As can be seen from Table 3, the values of U_0 obtained from the micromechanical AE model are within the range of 145–150 kJ/mole.

Since different structural rearrangements are observed at different levels of cyclic loading amplitude, the fatigue life was estimated only at the amplitude at which static tensile loading was performed and AE data were available to assess the fracture kinetics. Attempts to construct a fatigue curve based on the results of only one stress level of preliminary cycling lead to a large deviation from the real curve due to the high variability of the structural parameter γ. As indicated earlier, this parameter is affected by the loading regime. Hence, an important conclusion follows that to assess the lifetime of real objects

based on the results of AE tests, it is necessary to accurately estimate the equivalent level of the stress range amplitude in the operating cycle, corresponding to the non-stationary irregular stress range regime of the object.

It can be noted that for the specimens from the experiments conducted by other authors, the kinetic parameters X_{AE} и Y_{AE} showed stable values regardless of the degree of fatigue and loading rate. A crucial observation is that regardless of the degree of fatigue, all specimens demonstrated similar cumulative AE count dependencies, differing from each other only in the number of signals but not in the nature of the kinetics. In all three series of experiments, the parameter $\gamma/_{kT}$ was within a certain range (for example, for specimens made of steel 20, tested at a maximum stress in the cycle of 390, the parameter Y_{AE} did not exceed 0.0039–0.0054). This suggests the possibility of using these parameters to assess the lifetime at any moment during the operation of a real object and knowing the loading history to predict the remaining number of cycles to fracture.

According to the model, the basis for strength and durability control is the intensity of the stage of homogeneous elastoplastic destruction of the structural elements of the material, which can be traced at different scale levels. The nanoscale of the order of atomic bonds is described by the kinetic nature of fracture during thermal fluctuations under stress. Microscale tracking takes place using the kinetics of AE parameters and microcracking processes. The macro level is expressed in the number of completed loading cycles or the time sustained under the loading of the entire object or element before destruction.

The fracture process is divided into the stages of finely dispersed (scattered over the volume of the object or locally grouped in the area of the defect) microcracking, which includes the stages of heterogeneous and homogeneous fracture and localized macroscopic rupture. At the second stage, an enlarged localized discontinuity occurs (formation or growth of a crack), flowing elastically or plastically. The homogeneous stage is a period of stable "fracture" of structural elements of approximately the same strength, which proceeds until a critical concentration of microcracks accumulates. In the case of the cyclic loading of real pressure vessels in the concentrator area, during the achievement of a certain stress level, a similar "portion" of damage accumulates each cycle, namely the microcracks formed. This continues for most of the fatigue life, until a critical concentration of microcracks is reached during thermally activated microcrack formation and coalescence. The stage of stable damage accumulation corresponds to elastic plastic deformation, which is confirmed by the experimental results.

The decrease in temperature affects the value of the thermal activation parameters. Currently, the issues of the temperature dependence of the parameters included in the thermofluctuation fracture equation have been developed only from the standpoint of dislocation theory [60–62]. A decrease in the activation energy of fracture and the activation volume equally with a decrease in the deformation temperature in the low-temperature region was noted by several authors [63–65]. These two parameters are interconnected and describe the interaction of acting stresses and rupture fluctuations in the crystal lattice. The activation volume γ consists of the lattice expansion during the emergence of dislocations and the expansion during their movement or the volume of the kinetic unit. During their movement along slip planes, dislocations encounter obstacles with a short radius of action, such as impurity atoms, forest dislocations, or Peierls barriers, which they overcome with the help of thermal fluctuations [63]. To assess the nature of these barriers and the type of interaction with the dislocation, the rate and temperature sensitivity of the yield stress are determined, which are used to estimate the volume of the energy barrier. It is the distance between these obstacles that characterizes the type of barriers [63]. However, when the deformation temperature changes across the entire spectrum, the nature of the overcome barriers also changes and, as a consequence, the mechanism of body fracture.

As the temperature approaches absolute zero, the thermofluctuation component becomes smaller and smaller and at 0 K, it gives way to the athermal component, where fracture occurs only under the action of applied stresses [66]—this component is characterized by the yield strength at absolute zero [67]. Therefore, with a decrease in the fluctuation component, the area of influence on bond breaking by thermal vibrations decreases—the activation volume decreases, since the distance to the barrier has been reduced. As a result, the rate of bond breaking begins to be described by overcoming local barriers close to the dislocation, such as "forest" dislocations, which represent accumulations ("tangles") of randomly located dislocations. On the one hand, the intersection of such dislocations is associated with hardening during deformation and on the other hand, with a decrease in the focus of low-temperature fracture. When overcoming barriers (forest dislocations), part of the work is performed by stresses that "push" the dislocation to the barrier, and the other part by thermal fluctuations. In the work [61], the correspondence of the activation energy of fracture at low temperatures to the energy of intersection of "forest" dislocations for aluminum and the energy of formation of double kinks on screw dislocations for alpha-iron was confirmed. Thus, the decrease in the activation energy value is explained by a decrease in the area subjected to thermal fluctuation due to which the number of bonds involved in holding atoms in a given position is reduced and less energy is required to escape from the "potential well".

Certainly, it is necessary to consider fatigue life errors associated with the unaccounted influence of temperature during self-heating of the specimen and the temperature dependence of the kinetic parameters of durability. It has been repeatedly pointed out [68,69] that temperature fluctuations during cyclic loading can reach values exceeding the initial temperature by tens of degrees. However, heat removal from the specimens during low-temperature experiments (at $-60\ ^{\circ}C$) allowed for a more accurate fatigue life assessment. Furthermore, the rate of stress change during pressure fluctuations in real objects, due to its small magnitude, allows for neglecting the heating of the specimens.

Fatigue Life Evaluation Methodology

The methodology for assessing fatigue life under irregular loading is based on the following theoretical and practical principles:

1. The method for calculating the residual fatigue life of cryogenic vessels is based on the assessment of concentration kinetic parameters X_{AE} and Y_{AE}.
2. Vessels and pipelines for transporting and storing gasses should be inspected in their operating position. Acoustic emission diagnostics are implemented during static tests conducted according to the hydraulic/pneumatic testing program defined by the standards for AE inspection.
3. Placement of AE transducers on the object under inspection begins after the completion of preparatory work. Depending on the configuration of the object, material, the maximum distance between sensors, and the required accuracy of defect coordinate determination, the number and placement of transducers are determined.
4. The assessment of strength and structural parameters using the micromechanical AE model is as follows:
    - 4.1. During loading, using a diagnostic system, acoustic emission signals are automatically recorded with a set of standard parameters, namely cumulative AE count, AE activity, signal amplitude, etc. Simultaneously, the magnitude of the applied loading is recorded;
    - 4.2. During the post-processing of AE data, the time dependence of the logarithm of the cumulative AE count or other cumulative AE parameters (total energy, total amplitude, etc.) is plotted;

4.3. The time t_1 of the beginning of the uniform microcrack formation stage is recorded;

4.4. The time moments of the uniform fracture stage are registered according to kinetic (1), statistical (overlap coefficient, change in signal duration, etc.) (2), and the deformation stage feature (3);

4.5. For a more accurate assessment of the stress state of the stress concentrator source of AE for subsequent resource calculation, it is recommended to use a more complex technique based on the localization of AE signals. In this case, the flow of AE signals from the most dangerous zone of the object will be interpreted. This approach, using stress–strain state modeling with software, will allow for narrowing the range of theoretical stresses σ_{th} in the concentrator and thus the true stresses σ_t, which are used in Equation (34). This requires the use of a larger number of equipment channels and more complex software, but it provides more accurate assessments of the strength state for resource calculations;

4.6. The pressure in the vessel P_1 corresponding to the beginning of the uniform microcracking stage is recorded;

4.7. The stress–strain state of the vessel in a defect-free state is assessed at each time point of the tests, and the most stressed nodes are identified, as well as the scatter of stresses in the most stressed nodes (usually the junctions of flanges to shells and bends of vessel bottoms). This step can be performed in one of the possible software environments for stress–strain state assessment or by calculating the theoretical stresses σ_{th} in each node of the vessel (Figure 16).

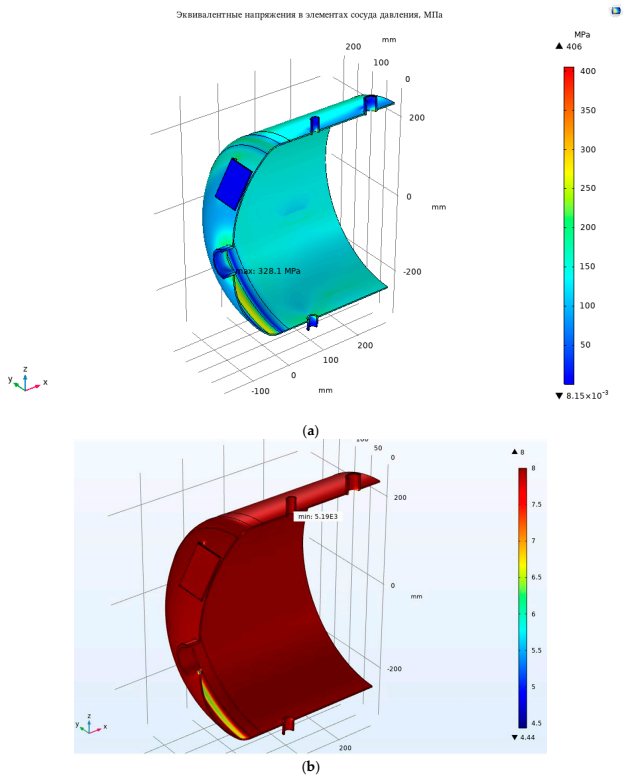

Figure 16. Results of modeling the stress state of the gas receiver under operating conditions: (**a**) stress distribution over the object's surface and maximum stresses in the area near the flange (as a natural stress concentrator); (**b**) results of the residual fatigue life calculation based on the low-cycle fatigue criterion using the Manson–Coffin model, taking into account the accumulation of plastic deformation.

5. Conducting tests on a series of flat laboratory specimens under conditions close to the test conditions (primarily observing the test temperature and loading rate). It is most desirable to use specimens obtained from the material of the vessel itself.
6. We find the average stress σ_t across the specimens, corresponding to the time moment t_1 of the beginning of the uniform microcracking stage in the specimens (Figure 17).

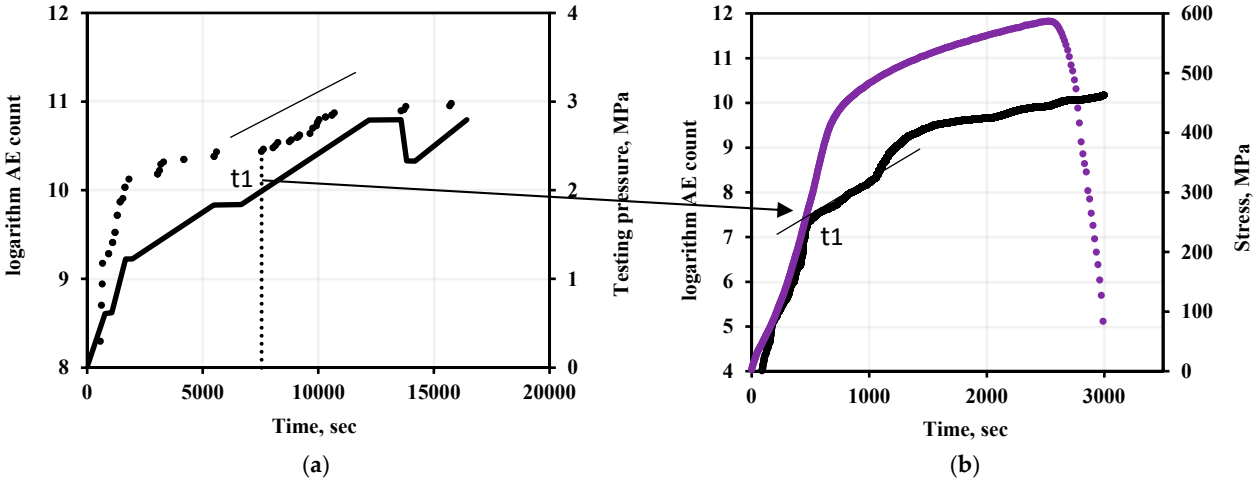

Figure 17. Example diagram for determining the range of acting stresses in the concentrator—the source of AE signals: (**a**) logarithm of the cumulative AE count and the pressure increase graph during hydraulic testing of the vessel [70]; (**b**) logarithm of the cumulative count and stress during the testing of laboratory specimens from the pressure vessel material (t_1—time moment of the beginning of the uniform microcracking stage).

7. Using the obtained stresses in the specimens σ_t and the real cryogenic vessel σ_{th} according to the simulation data, the stress concentration factor is found, which shows how much the real stresses exceed the theoretical ones in a vessel with a stress concentrator [71].

$$K = {}^{\sigma_t}/_{\sigma_{th}} \quad (38)$$

8. A series of true stress values σ_{ti} is calculated in the most dangerous zones of the vessel, taking into account stress concentration due to the presence of defects using the range of theoretical stresses σ_{th} obtained during stress–strain state modeling.
9. Using the time dependence of pressure in the vessel and the rate of true stress growth, parameters X_{AE} and Y_{AE} are determined, reflecting the individual structural features of the vessel, as well as the coefficient γ directly.
10. Using the obtained value of the structural parameter γ of the real vessel and the value of σ_t in the most dangerous (stressed) location of the tank, using Equation (34), the fatigue curve for the real vessel is plotted. The resulting fatigue curve expression is written for the most dangerous zone of the object—the developing concentrator.
11. Based on the information about the pressure drop modes in the vessel, an oscillogram of the pressure change over a certain operating period is plotted (Figure 18).
12. The oscillogram data are loaded into the corresponding Comsol Multiphysics software interface in the form of a drop in blocks, multiples of a given stress step (see Figure 19). The approach involves the use of the Structural Mechanics and Fatigue physics interfaces. Additional verification of the experimental results should be provided by assessing the stress–strain state of standard specimens for low- and high-cycle fatigue during testing under conditions close to the operation of a real vessel.

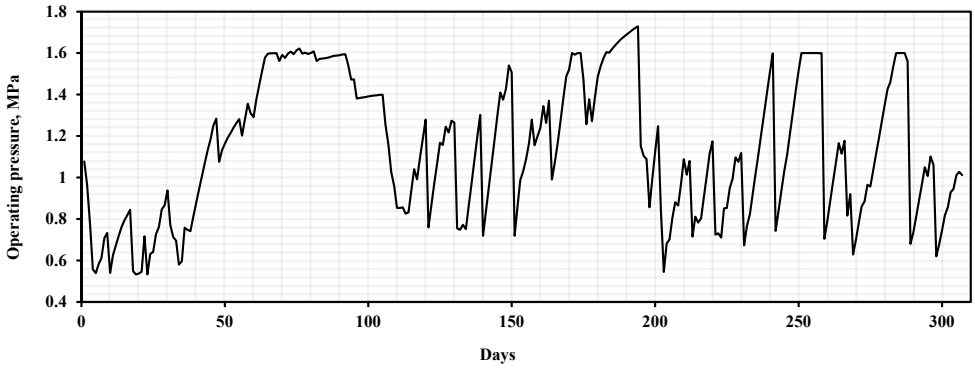

Figure 18. Operational data for converting pressure drop cycles in a liquid ethylene storage tank 47D01 into a fatigue curve relationship – pressure drop oscillogram over the course of a year.

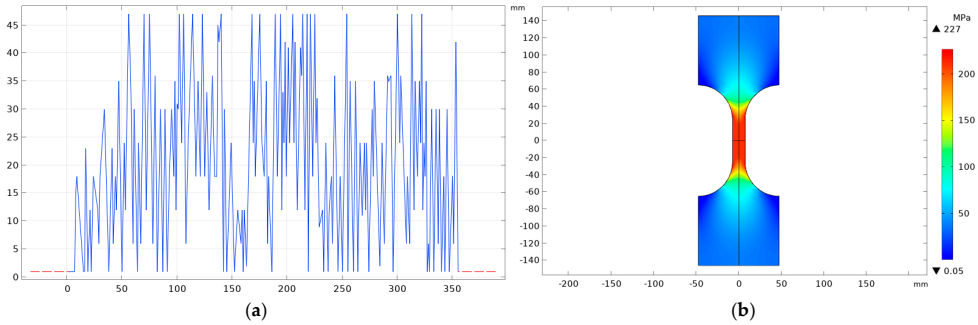

Figure 19. Simulation of the operational pressure drop process using laboratory AE testing of standard specimens and Comsol Multiphysics 5.6 software: (**a**) a graph of pressure changes in the tank during the year, modeled using the software; (**b**) stress–strain state of a standard specimen for low-cycle fatigue.

13. Using the Cumulative Damage interface and the embedded «rainflow» cycle counting algorithm, a matrix histogram of the distribution of operational loading cycles by stress range amplitude and the mean stress value is obtained, as well as a histogram of the relative contribution of these cycle groups to the overall damage of the structure (see Figure 20).
14. Groups of cycles with a certain ratio of amplitude value $\hat{\sigma}$ and mean cycle stress $\overline{\sigma}$ are identified, and their specific share in the total number of cycles is calculated.
15. Using Equation (34), the number of pressure drop cycles until vessel fracture is calculated for the block of cycles with the largest damaging share in the resource.
16. We use the Palmgren–Miner linear damage summation hypothesis to calculate the contribution of individual cycle groups to fracture.

$$\sum_{i=1}^{q} \frac{n_i}{N_i} = 1 \tag{39}$$

where q—number of loading blocks and N_i—total number of cycles to fracture under the action of a block with parameters $n_i, \hat{\sigma}_i$.

Obviously, the greatest damage is caused by cycles with the largest amplitude and sufficiently high mean cycle stress. With this tool, it is possible to recalculate the number of operational loading cycles based on the fatigue curve data, assuming that the response of the developing stress concentrator to the pressure drop corresponds to the given oscillogram. The latter is ensured by determining the moment in time when the uniform fracture stage begins. It follows that the number of cycles to fracture of a real structure, calculated by the maximum stress, will exceed the same for the fatigue curve due to the presence of a large number of practically "non-damaging" cycles of small amplitude.

The flowchart of the method implementation is shown in Figure 21.

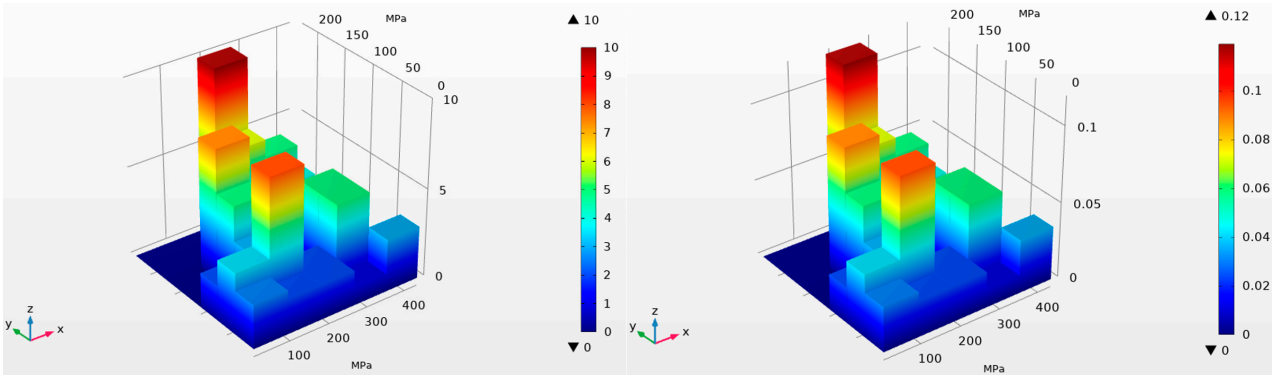

(**a**) (**b**)

Figure 20. Matrix histograms of the distribution of loading blocks of a real vessel (**a**) by stress amplitude $\hat{\sigma}$ and mean cycle stress $\overline{\sigma}$ and (**b**) by relative contribution to damage accumulation.

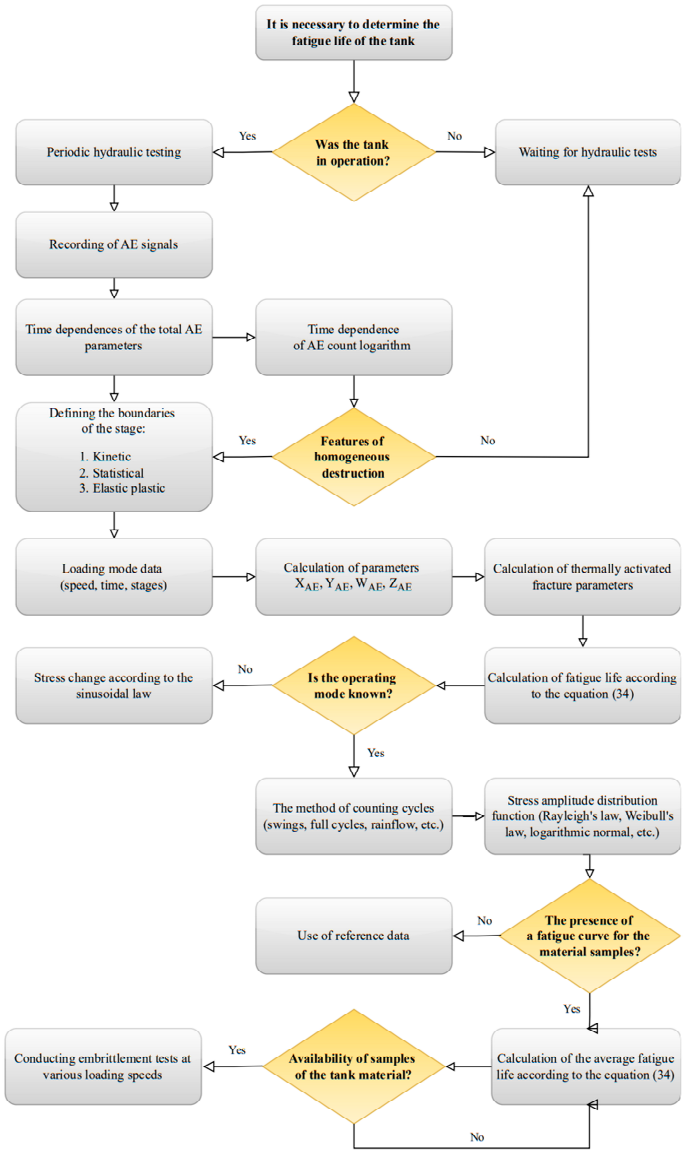

Figure 21. Flowchart of the method implementation.

5. Conclusions

In the first part of the article, an approach was proposed to assess the fatigue life of liquefied gas storage tanks using the acoustic emission method. The accumulation of microcracks was recorded using the time dependence of the total AE count. A model based on the equation of thermally activated Arrhenius-type fracture was proposed as a model of fatigue life. The time before microcrack formation at the stage of the elastoplastic deformation of structural steels was related to the arrival time of AE signals to the sensor. Thus, during loading of the specimens, the kinetics of microcrack formation were recorded, information about which is contained in the parameters X_{AE} and Y_{AE}. The structural parameter obtained during a single pre-fracture test was used in the thermally activated fracture equation, which was upgraded for cyclic loading. There are several conclusions that can be drawn as follows:

- The stage of elastoplastic deformation corresponds to the highest activity of acoustic emission and includes the stage of homogeneous microcrack formation, when areas with a similar structure become the place of microcrack formation;
- The kinetics of microcrack formation at the stage of elastoplastic deformation, studied using the AE method, is used to calculate fatigue life. The equation for calculating the number of cycles before fracture includes the structural parameter γ, which is a parameter of the individual structure of the material in the concentrator area. The values of γ can be obtained during single static tests;
- Numerical simulations confirm that the logarithmically normal and Weibull laws describe the distribution of the structural parameter γ well. The values obtained at the stage of homogeneous microcracking correspond to the "bell" of the distribution;
- To calculate the number of pressure drops in a tank for storage liquefied gasses during low-temperature operation, a method is proposed that includes the "rainflow" method for counting cycles, the time point at which the stage of homogeneous microcracking begins and the hypothesis of linear damage summation is confirmed.

Author Contributions: Conceptualization, V.V.N.; methodology, O.G.P. and V.V.N.; software, O.G.P.; validation, O.G.P. and V.V.N.; formal analysis, V.V.N.; data curation, O.G.P.; writing—original draft, O.G.P.; writing—review and editing, O.G.P.; visualization, O.G.P.; supervision, V.V.N.; project administration, V.V.N.; funding acquisition, O.G.P. and V.V.N. All authors have read and agreed to the published version of the manuscript.

Funding: This research received no external funding.

Data Availability Statement: The original contributions presented in this study are included in the article. Further inquiries can be directed to the corresponding author.

Conflicts of Interest: The authors declare no conflicts of interest.

Appendix A

Transformation of the Bessel Function of the First Kind of Zero Order $I_0(x) = {e^x}/{\sqrt{2\pi x}}$

For many practical problems in physics, the following differential equation is used:

$$J_n(z) = \frac{1}{2\pi}\int_0^{2\pi} cos(n\theta - zsin\theta)d\theta \quad \text{(A1)}$$

which, after some analytical transformations, is written in the general form of

$$z^2\frac{d^2y}{dz^2} + z\frac{dy}{dz} + \left(z^2 - n^2\right)y \quad \text{(A2)}$$

where $y = J_n(z)$ and the order n are integers. Thus, $J_n(z)$ is the solution to Equation (A1), and the parameter $J_n(z) = \frac{2}{n} A\pi$ is the Bessel function of the first kind of order n.

The complete solution of Equation (A2), by analogy with the differential equation for the potential difference, is written as

$$y = J_n(z)A_1 + Y_n(z)B_1 = y_1A_1 + y_2B_1 \tag{A3}$$

$J_n(z), Y_n(z)$—Bessel functions of the first and second kind and n—integer.

The Bessel function of integer order is defined as the solution to Equation (A2). $J_n(z)$ is related to the coefficient in a certain expansion such that the integer order $J_n(z)$ can be considered as a solution to the differential equation or a coefficient in an infinite series. For clarity, consider the zero-order function

$$\frac{d^2y}{dz^2} + \frac{1}{z}\frac{dy}{dz} + y = 0 \tag{A4}$$

To solve, we expand y into an infinite series as follows:

$$y = z^m\left(a_0 + a_1z + a_2z^2 + a_3z^3 + \dots\right) \tag{A5}$$

where m is the coefficient, and the parameters $a_0, a_1, a_2 \dots$ need to be determined. We substitute the resulting series into Equation (A3), and the series obtained by adding the first three terms of the series is equated to 0. Writing the algebra explicitly, we obtain

$$\frac{1}{2}\frac{dy}{dz} = z^m\left(a_0mz^{-2} + a_1(m+1)z^{-1} + a_2(m+2) + a_3(m+3)z + a_4(m+4)z^2 + \dots\right) \tag{A6}$$

$$\begin{aligned}\frac{d^2y}{dz^2} = z^m(a_0(m-1)mz^{-2} + a_1(m+1)mz^{-1} + a_2(m+2)(m+1) + a_3(m+2)(m+3)z \\ +a_4(m+3)(m+4)z^2 + \dots)\end{aligned} \tag{A7}$$

If the sum of the three series becomes 0, then the coefficients of the same order (power) z must also become 0. By equating the terms of the series to zero, we find the coefficients a_0, a_1, a_2, etc. Substituting the obtained coefficients into the series, we obtain

$$y_1 = a_0z^m\left\{1 - \frac{z^2}{(m+2)^2} + \frac{z^4}{(m+2)^2(m+4)^2} - \frac{z^6}{(m+2)^2(m+4)^2(m+6)^2} + \dots\right\} \tag{A8}$$

If Equation (A8) satisfies the expression above, then either a_0 or m must be equal to 0. Substituting $m = 0$ and $a_0 = 1$ we obtain

$$y_1 = J_0(z) = \left\{1 - \left(\frac{1}{2}z\right)^2 + \frac{\left(\frac{1}{2}z\right)^4}{(2!)^2} - \frac{\left(\frac{1}{2}z\right)^6}{(3!)^2} + \dots\right\} = \sum_{r=0}^{\infty}(-1)^r\frac{\left(\frac{1}{2}z\right)^{2r}}{(r!)^2} \tag{A9}$$

This series, absolutely convergent for all values of z real or complex, is the first solution to Equation (A2) and is defined as the Bessel function of the first kind of zero order, denoted as $J_0(z)$ and identical to Equation (A2) when $n = 0$.

The second independent solution y_2, together with the first, constitutes a fundamental system. There are various forms of the second solution, one of which (Neumann's method) is found by the expansion used to determine the first solution. Neumann's Bessel function of the second kind of zero order is

$$\begin{aligned} y_2 = Y_0(z) &= logz \cdot J_0(z) + \left\{ \left(\tfrac{1}{2}z\right)^2 - \frac{\left(\frac{1}{2}z\right)^4}{(2!)^2}\left(1+\tfrac{1}{2}\right) + \frac{\left(\frac{1}{2}z\right)^6}{(3!)^2}\left(1+\tfrac{1}{2}+\tfrac{1}{3}\right) - \ldots \right\} \\ &= logz \cdot J_0(z) - \sum_{r=1}^{\infty} (-1)^r \frac{\left(\frac{1}{2}z\right)^{2r}}{(r!)^2}\left\{1+\tfrac{1}{2}+\tfrac{1}{3}+\ldots+\tfrac{1}{r}\right\} \end{aligned} \tag{A10}$$

Then, the complete solution, given condition $y_1 y_2{}' - y_2 y_1{}' \neq 0$ (linearly independent) using the obtained solutions, is written as

$$y = J_0(z)A_1 + Y_0(z)B_1 \tag{A11}$$

For many practical engineering problems, z in Equation (A11) is replaced by zi, which gives the modified (or hyperbolic) Bessel equation. Then, it can be solved using the rewritten equations.

$$y = J_v(zi)A_1 + Y_{-v}(z)B, \quad v \neq n \tag{A12}$$

$$y = J_n(zi)A_1 + Y_n(z)B \tag{A13}$$

However, this form is inconvenient, and a representation of the solution in real rather than complex form is usually desired. According to Euler's formula,

$$\pm z(cos\varphi + isin\varphi) = \pm ze^{i\varphi} \tag{A14}$$

$$\pm zi\left(\frac{1}{i}cos\varphi + sin\varphi\right) = \pm ze^{i\varphi} \tag{A15}$$

For $\varphi = {}^{\pi}/_{2}$, the condition $i^{-v} = e^{-\frac{1}{2}v\pi i}$ is satisfied, which is a constant for the order v. Then, for real z, the modified Bessel function of the first kind of order v is

$$I_v(z) = i^{-v}J_v(zi) \tag{A16}$$

Or

$$I_v(z) = {e^{\pm v\pi i/2}}\Big/{J_v\left(ze^{\pm \pi i/2}\right)} \tag{A17}$$

For integer order, one can write

$$I_n(z) = i^{-n}J_n(zi) \tag{A18}$$

The existing linearly independent solution is shown in the following equation:

$$I_n(z) = J_{-n}(z) \tag{A19}$$

The Bessel function written using the Gamma function looks like

$$J_n(z) = \frac{\left(\frac{1}{2}z\right)^v}{\sqrt{\pi}\,\Gamma\left(v+\frac{1}{2}\right)}\int_0^{\pi} e^{\pm izcos\theta} sin^{2v}\theta d\theta \tag{A20}$$

For complex numbers, we write

$$I_n(z) = i^{-v}J_v(zi) = \frac{\left(\frac{1}{2}z\right)^v}{\sqrt{\pi}\,\Gamma\left(v+\frac{1}{2}\right)}\int_0^{\pi} e^{\pm zcos\theta} sin^{2v}\theta d\theta \tag{A21}$$

The modified Bessel function of the first kind is often used in various stochastic (noise) processes, physical systems, and communications. In these practical cases, the functions for

real values x of the argument z and integer order n are usually represented by an integral. For zero order and also considering that $\Gamma\left(\frac{1}{2}\right) = \sqrt{\pi}$, we obtain

$$I_0(x) = \frac{1}{\pi}\int_0^{\pi} e^{xcos\theta} d\theta y = J_0(z)A_1 + Y_0(z)B_1 \quad \text{(A22)}$$

$$I_n(x) = \frac{1}{\pi}\int_0^{\pi} e^{xcos\theta} cos\theta d\theta \quad \text{(A23)}$$

This function has a monotonic characteristic, increasing with increasing argument x rather than a sinusoidal characteristic $J_v(z)$. The integral $I_n(x)$ cannot be expressed explicitly. Polynomial approximation methods are used for the solution. In the work [49], numerical integration with an alternative power series expansion for small x and asymptotic relations in series for large x is proposed.

The integral (A23) is not convenient for direct evaluation and is more appropriately solved by expansion into a convergent series. An asymptotic expansion $I_0(x)$ is used to obtain an approximation using a series in the form of

$$u = 1 + \frac{c1}{x} + \frac{c2}{x^2} + \frac{c3}{x^3} + \ldots \quad \text{(A24)}$$

And the solution for $u - e^x = yx^{0.5}$ is presented in the modified Bessel equation of zero order. For large and positive x, this is written as

$$I_0(x) = \frac{e^x}{\sqrt{2\pi x}}\left\{1 + \frac{1^2}{1!8x} + \frac{1^2 3^2}{2!(8x)^2} + \frac{1^2 3^2 5^2}{3!(8x)^3} + \ldots\right\} \quad \text{(A25)}$$

Despite the fact that the series is divergent, the sum of the first few terms gives values close to $I_0(x)$, especially for large x. For $x = 10$ with a series of eight terms, the error is less than $2{\cdot}10^{-8}$.

Since the absolute size of the series terms rapidly decreases, the relative error decreases with an increasing value of x. Then, for a given error and the smallest x, it is possible to determine the number of series terms that need to be considered when applying the function. Then, Equation (A25) for large values of the argument (the series components approach one as x increases) can be reduced to

$$I_0(x) = \frac{e^x}{\sqrt{2\pi x}} \quad \text{(A26)}$$

References

1. Podoprigora, D.G.; Byazrov, R.R.; Lagutina, M.A.; Arabov, D.V.; Galimov, V.V.; Ermolin, D.S. A novel integrated methodology for screening, assessment and ranking of promising oilfields for polymer floods. *Adv. Geo-Energy Res.* **2024**, *12*, 8–21. [CrossRef]
2. Dvoynikov, M.V.; Minaev, Y.D.; Minibaev, V.V.; Kambulov, E.Y.; Lamosov, M.E. Technology for killing gas wells at managed pressure. *Bull. Tomsk. Polytech. Univ. Geo Assets Eng.* **2024**, *335*, 7–18. [CrossRef]
3. Myakotnykh, A.A.; Ivanova, P.V.; Ivanov, S.L. Criteria and technological requirements for creation of a bridge platform to extract peat raw materials for climate-neutral geotechnology. *Gorn. Promyshlennost* **2024**, *4*, 116–120. (In Russian) [CrossRef]
4. Zemenkova, M.; Chizhevskaya, E.; Zemenkov, Y. Intelligent monitoring of the condition of hydrocarbon pipeline transport facilities using neural network technologies. *J. Min. Inst.* **2022**, *258*, 933–944. [CrossRef]
5. Didmanidze, O.; Afanasev, A.; Khakimov, R. Mathematical model of the liquefied methane phase transition in the cryogenic tank of a vehicle. *J. Min. Inst.* **2020**, *243*, 337–347. [CrossRef]
6. Pshenin, V.; Zakirova, G. Improving the efficiency of oil vapor recovery units in the commodity transport operations at oil terminals. *J. Min. Inst.* **2024**, *265*, 121–128. [CrossRef]

7. Dzhemilev, E.; Shammazov, I.; Sidorkin, D.; Mastobaev, B.; Gumerov, A. Developing technology and device for the main pipelines repair with cutting out their defective sections. *Neft. Khozyaystvo* **2022**, *10*, 78–82. [CrossRef]
8. Gendler, S.G.; Stepantsova, A.Y.; Popov, M.M. Justification on the safe exploitation of closed coal warehouse by gas factor. *J. Min. Inst.* **2024**, 1–11, EDN SIJDWE. Available online: https://pmi.spmi.ru/pmi/article/view/16519 (accessed on 4 January 2025).
9. Bickell, M.B.; Ruiz, C. *Pressure Vessel Design and Analysis*, 1st ed.; Red Globe Press: London, UK, 1967.
10. Singh, K.P.; Soler, A.I. *Mechanical Design of Heat Exchangers and Pressure Vessel Components*; Springer: Berlin/Heidelberg, Germany, 1984; ISBN 978-3-662-12443-7.
11. Li, Y.; Wang, J.; Sun, Z. Application of low-cycle fatigue data to pressure vessel design fatigue curve. *Int. J. Fatigue* **1990**, *12*, 215–218. [CrossRef]
12. Aistov, A.S.; Makovkin, G.A. Investigation of low cycle fatigue of pipes of main gas and oil pipelines. *Sci. Probl. Water Transp.* **2008**, 149–159.
13. Nikolaev, A.; Goluntsov, A.; Breff, A. Determination of the coefficient of hydraulic resistance when using anti-turbulence additives. *Reliab. Theory Appl.* **2024**, *19*, 107–124. [CrossRef]
14. Sarkar, A.; Kumawat, B.K.; Chakravartty, J.K. Low cycle fatigue behavior of a ferritic reactor pressure vessel steel. *J. Nucl. Mater.* **2015**, *462*, 273–279. [CrossRef]
15. Effect of loading wave form on the results of low cycle fatigue and fatigue crack propagation tests. In *Low Cycle Fatigue and Elasto-Plastic Behaviour of Materials*; Portella, P.D., Rie, K.-T., Eds.; Elsevier: Oxford, UK, 1988.
16. Keith, E. *Pressure Vessel and Stacks Field Repair Manual*; Butterworth-Heinemann: Oxford, UK, 2008.
17. Vladimirov, V.I.; Orlov, A.N. Thermal activation of microcrack nucleation in crystals. *Strength Mater.* **1971**, *3*, 154–156. [CrossRef]
18. Ortiz, M. Microcrack coalescence and macroscopic crack growth in brittle solids. *Int. J. Solids Struct.* **1988**, *24*, 231–250. [CrossRef]
19. Bolshakov, A.M.; Andreev, Y.M. Fracture analysis of metal structures functioned in the north conditions. *AMaT* **2015**, *12*, 27–31. [CrossRef]
20. Palaev, A.G.; Krasnikov, A.A. Ultrasonic Treatment of Welded Joint from External, Internal and Two Sides on Reduction of Residual Welding Stresses. *IJE* **2024**, *37*, 2171–2180. [CrossRef]
21. Investigation of the operability, reliability, and cold resistance of metal structures and their welded joints operating in the Far North and the Arctic. In *Safety and Survivability of Technical Systems: Materials and Reports: In 3 Volumes*; Bolshakov, A.M., Sleptsov, O.I., Eds.; Siberian Federal University: Krasnoyarsk, Russian, 2015.
22. Hectors, K.; De Waele, W. Cumulative Damage and Life Prediction Models for High-Cycle Fatigue of Metals: A Review. *Metals* **2021**, *11*, 204. [CrossRef]
23. Rege, K.; Pavlou, D.G. A one-parameter nonlinear fatigue damage accumulation model. *Int. J. Fatigue* **2017**, *98*, 234–246. [CrossRef]
24. Regel', V.R.; Slutsker, A.I.; Tomashevskii, E.E. The kinetic nature of the strength of solids. *Uspekhi Fiz. Nauk* **1972**, *106*, 193–228. [CrossRef]
25. Mishnaevsky, L.; Brøndsted, P. Modeling of fatigue damage evolution on the basis of the kinetic concept of strength. *Int. J. Fract.* **2007**, *144*, 149–158. [CrossRef]
26. Mahmoudi, A.; Khonsari, M.M. Evaluation of fatigue in unidirectional and cross-ply laminated composites using a coupled entropy-kinetic concept. *J. Compos. Mater.* **2022**, *56*, 2443–2454. [CrossRef]
27. Doh, J.; Lee, J. Bayesian estimation of the lethargy coefficient for probabilistic fatigue life model. *J. Comput. Des. Eng.* **2018**, *5*, 191–197. [CrossRef]
28. Hur, S.H.; Doh, J.; Yoo, Y.; Kim, S.-W.; Lee, J. Stress-life prediction of 25 °C polypropylene materials based on calibration of Zhurkov fatigue life model. *Fatigue Fract. Eng. Mater. Struct.* **2020**, *43*, 1784–1799. [CrossRef]
29. Han, Z.; Luo, H.; Sun, C.; Li, J.; Papaelias, M.; Davis, C. Acoustic emission study of fatigue crack propagation in extruded AZ31 magnesium alloy. *Mater. Sci. Eng. A* **2014**, *597*, 270–278. [CrossRef]
30. Doh, J.; Byun, J.; Lee, J. Bayesian approach for the lethargy coefficient estimation in the probabilistic creep-fatigue life model. *Annu. Conf. PHM Soc.* **2016**, *8*, 1–8. [CrossRef]
31. Nikonov, Y.A. Fatigue strength of solids from the standpoint of the kinetic concept of destruction. In *Leningrad Polytechnic Institute*; M.I. Kalinin Institute: Leningrad, Russian, 1975.
32. Song, J.H.; Noh, H.G.; Yu, H.S.; Kang, H.Y.; Yang, S.M. Estimation of fatigue life by lethargy coefficient using molecular dynamic simulation. *Int. J. Automot. Technol.* **2004**, *5*, 215–219.
33. Moghanlou, M.R.; Khonsari, M.M. On the kinetic formulation of fracture fatigue entropy of metals. *Fatigue Fract. Eng. Mater. Struct.* **2022**, *45*, 565–577. [CrossRef]
34. Petrov, V.A. *The Physical Foundations of Forecasting the Durability of Structural Materials*; Petrov, V.A., Bashkarev, A.Y., Vettegren, V.I., Eds.; Polytechnic: St. Petersburg, Russian, 1993; p. 475.
35. Fukagawa, M.; Kohno, T.; Murayama, T.; Kaihara, S. Safety Requirements for Cryogenic Storage Tank and COD Characteristics of the Welded Joint with Partially Embrittled Rrgion. *Trans. Iron Steel Inst. Jpn.* **1984**, *24*, 1072–1081. [CrossRef]

36. Goritskii, V.M. A criterion of fracture of steels susceptible to propagation of brittle microcracks along crystal boundaries. *Strength Mater.* **1987**, *19*, 479–486. [CrossRef]
37. Krasovskii, A.Y. Ductile-to-brittle transition temperature as a measure of the crack resistance of steels. *Strength Mater.* **1985**, *17*, 1439–1446. [CrossRef]
38. Scibetta, M.; Ferreño, D.; Gorrochategui, I.; Lacalle, R.; van Walle, E.; Martín, J.; Gutiérrez-Solana, F. Characterisation of the fracture properties in the ductile to brittle transition region of the weld material of a reactor pressure vessel. *J. Nucl. Mater.* **2011**, *411*, 25–40. [CrossRef]
39. Hartmaier, A.; Gumbsch, P. On the activation energy forthe brittle-ductile transition. *Phys. Status Solidi B Basic Res.* **1997**, *202*, R1–R2. [CrossRef]
40. *GOST 25.506*; Design, Calculation and Strength Testing. Methods of Mechanical Testing of Metals. Determination of Fracture Toughness Characteristics Under the Static Loading. IKP Publishing House of Standards: Moscow, Russia, 1985.
41. *BS ISO 12135:2021*; Metallic Materials. Unified Method of Test for the Determination of Quasistatic Fracture Toughness. ISO: Geneva, Switzerland, 2021.
42. Trushko, V.L.; Rozanov, A.O.; Saitgaleev, M.M.; Petrov, D.N.; Ilinov, M.D.; Karmanskii, D.A.; Selikhov, A.A. Acoustic emission criteria for analyzing the process of rock destruction and evaluating the formation of fractured reservoirs at great depths. *J. Min. Inst.* **2024**, *269*, 848–858, EDN EGOJFL.
43. Takanori, O.; Pao, Y.-H. Microcrack initiation and acoustic emission during fracture toughness tests of A533B steel. *Metall. Trans. A* **1986**, *17A*, 843–852. [CrossRef]
44. Barat, K.; Bar, H.N.; Mandal, D.; Roy, H.; Sivaprasad, S.; Tarafder, S. Low temperature tensile deformation and acoustic emission signal characteristics of AISI 304LN stainless steel. *Mater. Sci. Eng. A* **2014**, *597*, 37–45. [CrossRef]
45. Freed, A.D.; Leonov, A.I. The Bailey criterion: Statistical derivation and applications to interpretations of durability tests and chemical kinetics. *Math. Phys.* **2002**, *53*, 160–166. [CrossRef]
46. Petrov, V.A. Durability of solids under low loadings, non-destructive stresses. *Solid State Phys.* **1984**, *26*, 2116–2119.
47. Petrov, V.A. Dilaton model of thermofluctuational crack nucleation. *Solid State Phys.* **1983**, *25*, 3124–3127.
48. Petrov, M.G.; Ravikovich, A.I. Accumulation of damage during plastic deformation and creep of aluminum alloys. *Appl. Mech. Tech. Phys.* **2006**, *47*, 172–182. [CrossRef]
49. Brewster Geelen, B.D. Accurate solution for the modified Bessel faction of the first kind. *Adv. Eng. Softw.* **1995**, *23*, 105–109. [CrossRef]
50. Zaitsev, M.G. Statistical modeling of clustering of stable microcracks in solids. *Solid State Phys.* **1985**, *27*, 3653–3661.
51. Strizhalo, V.A. *Cyclic Strength and Creep of Metals Under Low-Cycle Loading at Low and High Temperatures*; Naukova Dumka: Kiev, Ukraine, 1978.
52. Botvina, L.R.; Kushnarenko, V.M.; Tyutin, M.R. Fracture stages and residual strength of pipe steel after long-term operation. *Phys. Mesomech.* **2021**, *24*, 50–61. [CrossRef]
53. Botvina, L.R.; Tyutin, M.R.; Levin, V.P.; Ioffe, A.V.; Perminova, Y.S.; Prosvirnin, D.V. Mechanical and Physical Properties, Fracture Mechanisms, and Residual Strength of 15Kh2GMF Steel for Oil Sucker Rods. *Russ. Metall.* **2021**, *2021*, 546–558. [CrossRef]
54. Botvina, L.R.; Tyutin, M.R.; Bolotnikov, A.I.; Petersen, T.B. Effect of Preliminary Cycling on the Acoustic Emission Characteristics of Structural 15Kh2GMF Steel. *Russ. Metall.* **2021**, *2021*, 32–41. [CrossRef]
55. Botvina, L.R.; Tyutin, M.R.; Petersen, T.B.; Levin, V.P.; Soldatenkov, A.P.; Prosvirnin, D.V. Residual Strength, Microhardness, and Acoustic Properties of Low-Carbon Steel after Cyclic Loadinging. *J. Mach. Manuf. Reliab.* **2018**, *47*, 516–524. [CrossRef]
56. Botvina, L.R.; Tyutin, M.R.; Petersen, T.B.; Prosvirnin, D.V.; Morozov, A.E.; Kolokolov, E.I. Residual Strength of Cyclically Deformed Corrosion-Resistant Steel. *Russ. Metall.* **2020**, *2020*, 483–492. [CrossRef]
57. Valiev, A.S.; Kuzeev, I.R. Assessment of the degree of damage to 09G2C steel specimens exposed to low-cycle fatigue by acoustic emission control method. *Oil Gas Bus.* **2022**, *20*, 142. [CrossRef]
58. Botvina, L.R. Damage evolution on different scale levels. *Izv. Phys. Solid Earth* **2011**, *47*, 859–872. [CrossRef]
59. Perveitalov, O.G.; Nosov, V.V.; Schipachev, A.M.; Alekhin, A.I. Thermally Activated Crack Growth and Fracture Toughness Evaluation of Pipeline Steels Using Acoustic Emission. *Metals* **2023**, *13*, 1272. [CrossRef]
60. Loginov, B.M.; Proskurnin, A.N.; Vershinin, E.V. Patterns of dislocation movement through ensembles of dislocations of forests and point obstacles in conditions of simultaneous action of static and cyclic loadinging. *Solid State Phys.* **2002**, *44*, 1885–1888. [CrossRef]
61. Petrov, A.I.; Razuvaeva, M.V. Evaluation of fracture activation parameters in aluminum and α-iron based on durability measurements at moderate and low temperatures. *J. Tech. Phys.* **2010**, *80*, 90–95.
62. Petrov, M.G. Investigation of the longevity of materials on the basis of the kinetic concept of fracture. *J. Appl. Mech. Tech. Phys.* **2021**, *62*, 145–156. [CrossRef]
63. Malygin, G.A. Analysis of the velocity sensitivity of the flow stresses of nanocrystalline metals with FCC and BCC gratings. *Solid State Phys.* **2007**, 49.

64. Campbell, J.D.; Ferguson, W.G. The temperature and strain-rate dependence of the shear strength of mild steel. *Philos. Mag.* **1970**, *21*, 63–82. [CrossRef]
65. Weaver, J.L.; Beatty, C.L. The effect of temperature on compressive fatigue of polystyrene. *Polym. Eng. Sci.* **1978**, *18*, 1117–1126. [CrossRef]
66. Firstov, S.O.; Rogul, T.G. Thermoactivation Analysis of the Flow-Stress–Temperature Dependence in the F.C.C. Solid Solutions. *Metallofiz. Noveishie Tekhnol.* **2017**, *39*, 33–48. [CrossRef]
67. Morris, D.G. Strengthening mechanisms in nanocrystalline metals. In *Nanostructured Metals and Alloys*; Woodhead Publishing: Sawston, UK, 2011; pp. 299–328.
68. Kireenko, O.F.; Leksovskii, A.M.; Regel, V.R. Role of heating in connection with the reduced life of cyclically stressed polymers. *Polym. Mech.* **1968**, *4*, 483–488. [CrossRef]
69. Stepanov, V.A.; Nikonov, Y.A.; Timoshenko, I.I. Influence of cyclic loading conditions on the life of materials. *Strength Mater.* **1979**, *11*, 575–577. [CrossRef]
70. Mukhopadhyay, C.K.; Haneef, T.K.; Rao, B.P.C.; Jayakumar, T. Condition monitoring of exchange towers of heavy water plant during hydrotesting by acoustic emission technique. *Insight-Non-Destr. Test. Cond. Monit.* **2011**, *53*, 29–33. [CrossRef]
71. Pilkey, W.D.; Pilkey, D.F. *Peterson's Stress Concentration Factors*, 4th ed.; John Wiley & Sons Inc.: Hoboken, NJ, USA, 2020; ISBN 9781119532514.

Disclaimer/Publisher's Note: The statements, opinions and data contained in all publications are solely those of the individual author(s) and contributor(s) and not of MDPI and/or the editor(s). MDPI and/or the editor(s) disclaim responsibility for any injury to people or property resulting from any ideas, methods, instructions or products referred to in the content.